

POLITECNICO DI TORINO

Corso di Laurea in Ingegneria Biomedica

Tesi di Laurea Magistrale

**Experimental methods for measuring
the mechanical properties of soft
tissues under large deformations**



Relatori

Luigi Preziosi
Valentina Balbi

Candidato

Nicola Bottasso

Marzo 2020

Ai miei genitori e a Cristina.

Abstract

The work is focused on the elastic properties of soft tissues, as the brain. Agar gels are tested through a rheometer: in particular cylindrical samples of different diameters undergo a torsion test, obtaining torque and normal force required to twist the samples at constant rotation velocity. These constitutive parameters are useful to determine the constitutive model for better fitting experimental data. The gels are modelled with Mooney-Rivlin equations, highlighting the presence of a positive Poynting effect, i.e. they expands in the direction perpendicular to the plane of twisting. Once the Mooney-Rivlin parameters (C_1 and C_2) and the *shear modulus* μ are figured out, they are used to implement a Finite Element simulation in Abaqus and then experimental, theoretical and numerical data are compared.

The final goal of this research is the development of a FE model able to analyse more complex deformations with high accuracy and improve the knowledge about the Traumatic Brain Injury, an underestimated pathology affecting a large part of the population.

Contents

List of Figures	III
List of Tables	V
Introduction	1
1 Traumatic Brain Injury	3
1.1 Notions on the brain	4
1.2 Traumatic Brain Injury	5
1.2.1 Classification and symptoms	6
1.2.2 Causes, incidence on population and socio-economic impact	8
2 Nonlinear Elasticity	11
2.1 Kinematics	13
2.1.1 Bodies, configurations and motions	13
2.1.2 Deformation Gradient	14
2.1.3 Deformation of line, area and volume elements	15
2.1.4 Measures of strain	16
2.2 Balance laws and governing equations of motion	16
2.2.1 Mass conservation	16
2.2.2 Balance of linear and angular momentum	17
2.2.3 Cauchy's theorem	18
2.3 Constitutive equations	19
2.3.1 Isotropic hyperelasticity	20
2.3.2 Incompressible elastic materials	20
2.3.3 Examples of strain energy functions	21
3 Materials and methods	23
3.1 Brain mechanical testing techniques	23
3.2 Testing procedure	26
3.2.1 Agar gels	26
3.2.2 Equipment and protocol	28

3.2.3	Testing issues	30
4	Experimental results	33
4.1	Summary of the results	33
4.2	Choice of the model and filtering procedure	35
4.3	Filtered data	36
4.3.1	Comments	38
5	Modelling	41
5.1	Theory	41
5.1.1	Choice of the strain energy function	43
5.1.2	Analytic expression of torque and normal force	45
5.2	Parameters estimation	45
5.3	Computational validation	48
5.3.1	Procedure	49
5.3.2	Results	51
6	Conclusions	55
	Acknowledgements	59
	Bibliografia	61

List of Figures

1.1	Impact direction, kinematics, skull stress (maximum Von Mises stress for skull bone) and brain strain (maximum Green-Lagrange strain) for radial (upper) and oblique (lower) impact at same collision speed of 6.7 m/s [6].	3
1.2	Schematic representation of the brain anatomy [9].	5
1.3	Estimated percentage of TBI causes in USA from 2002 to 2006 [22].	9
1.4	Annual rate of TBI related with age groups [23].	9
2.1	Typical stress-strain response curve in tensile tests of a metal [27]. .	11
2.2	Typical stress-strain response curve in tensile tests of a soft tissue [27].	11
2.3	Typical stress-strain response curve in tensile tests of a rubber [27].	12
2.4	Reference configuration B_r and current configuration B_t with position vectors X and x of a material point P [29].	13
2.5	Infinitesimal line elements at X on the surface S_r in the reference configuration B_r and their images at x on the deformed surface S_t in the current configuration B_t	15
2.6	Stress vector $t_{(n)}$ at a point of the surface S where the unit normal is n .	17
3.1	MRE testing representation [31].	24
3.2	Sketch of the experimental set-up suitable for tension tests of soft tissues [33].	24
3.3	Standard testing protocols for soft solids applied to brain matter: (a) tensile, (b) compression, (c) simple shear and (d) torsion tests [4].	25
3.4	Comparison of stress-strain curves of different gels and brain matter at 10/s strain rate deriving from uniaxial compression tests, from a study by Pervin and Chen [35].	26
3.5	(a) Example of a 3D printed mould with 20, 15 and 10 mm diameters holes in which the hot gel is poured; (b) 3D printed cutting guide: the sample is placed inside and is cut with a scalpel.	27
3.6	Cylindrical 2% agar gels of 25, 20 and 15 mm diameters ready for testing.	27
3.7	Anton Paar rheometer.	28

3.8	(a) "Set zero gap" procedure: the upper plate touches the bottom plate; (b) the sample is glued and ready for twisting.	29
3.9	Example of a broken sample after the test.	30
3.10	Example of a not centred sample.	31
4.1	Typical output of the rheometer for (a) torque and (b) normal force, in which it is possible to identify an initial linear region.	35
4.2	(a) Filtered torque τ vs twist ϕ and (b) normal force N_z vs twist squared ϕ^2 for 25 mm diameter samples.	36
4.3	(a) Filtered torque τ vs twist ϕ and (b) normal force N_z vs twist squared ϕ^2 for 20 mm diameter samples.	36
4.4	(a) Filtered torque τ vs twist ϕ and (b) normal force N_z vs twist squared ϕ^2 for 15 mm diameter samples.	37
4.5	(a) Filtered torque τ vs twist ϕ and (b) normal force N_z vs twist squared ϕ^2 for 10 mm diameter samples.	37
4.6	(a) Mean torque and standard deviation and (b) mean normal force and standard deviation for all geometries.	38
5.1	Schematic representation of the simple torsion of a cylinder with initial radius R_0 and height H_0 and final radius r_0 and height h_0 , in cylindrical coordinates; torque and normal force are also displayed.	41
5.2	Example of fitting for (a) torque and (b) normal force of a 25 mm diameter sample.	46
5.3	Creation of a cylinder on Abaqus.	49
5.4	Coupling of the top surface of the cylinder to the reference point.	50
5.5	Example of mesh on Abaqus.	50
5.6	25 mm diameter sample S_3 : comparison of (a) torque and (b) normal force between experimental data (blue circles), numerical simulations (green triangles) and "theory" (red solid line).	51
5.7	20 mm diameter sample S_7 : comparison of (a) torque and (b) normal force between experimental data (blue circles), numerical simulations (green triangles) and "theory" (red solid line).	52
5.8	15 mm diameter sample S_5 : comparison of (a) torque and (b) normal force between experimental data (blue circles), numerical simulations (green triangles) and "theory" (red solid line).	52
5.9	10 mm diameter sample S_6 : comparison of (a) torque and (b) normal force between experimental data (blue circles), numerical simulations (green triangles) and "theory" (red solid line).	53
6.1	Scatter plot of (a) μ and (b) C_2 , for every sample diameter group.	55
6.2	Box plots of (a) μ and (b) C_2 , for every sample diameter group.	56

List of Tables

1.1	Injury classifiers.	7
4.1	Actual height, deflection angle and twist at the breaking point, with relative mean and standard deviation, for each sample of the 25 mm diameter geometry.	33
4.2	Actual height, deflection angle and twist at the breaking point, with relative mean and standard deviation, for each sample of the 20 mm diameter geometry.	34
4.3	Actual height, deflection angle and twist at the breaking point, with relative mean and standard deviation, for each sample of the 15 mm diameter geometry.	34
4.4	Actual height, deflection angle and twist at the breaking point, with relative mean and standard deviation, for each sample of the 10 mm diameter geometry.	34
4.5	Mean strains in radians at the break point for each sample geometry.	38
5.1	Estimated elastic parameters for 25 mm diameter samples: Mooney-Rivlin parameter C_2 , the shear modulus μ , the stretching ratio λ and the coefficients of determination for torque R_τ^2 and normal force R_N^2 ; in the last row, mean and standard deviation for C_2 and μ are evaluated.	47
5.2	Estimated elastic parameters for 20 mm diameter samples: Mooney-Rivlin parameter C_2 , the shear modulus μ , the stretching ratio λ and the coefficients of determination for torque R_τ^2 and normal force R_N^2 ; in the last row, mean and standard deviation for C_2 and μ are evaluated.	47
5.3	Estimated elastic parameters for 15 mm diameter samples: Mooney-Rivlin parameter C_2 , the shear modulus μ , the stretching ratio λ and the coefficients of determination for torque R_τ^2 and normal force R_N^2 ; in the last row, mean and standard deviation for C_2 and μ are evaluated.	48

5.4	Estimated elastic parameters for 10 mm diameter samples: Mooney-Rivlin parameter C_2 , the shear modulus μ , the stretching ratio λ and the coefficients of determination for torque R_t^2 and normal force R_N^2 ; in the last row, mean and standard deviation for C_2 and μ are evaluated.	48
5.5	Time increments for Abaqus simulations.	49
5.6	Details of the mesh for each geometry tested.	50
6.1	Obtained p-values comparing μ for every pair of sample diameter groups; 10, 15,20 and 25 indicate 10 mm, 15 mm, 20 mm and 25 mm sample diameter groups.	56
6.2	Obtained p-values comparing of C_2 for every pair of sample diameter groups; 10, 15,20 and 25 indicate 10 mm, 15 mm, 20 mm and 25 mm sample diameter groups.	57

Introduction

The purpose of the mechanical study of biological tissues, such as the brain, is the development of Finite Element models, able to predict the behaviour of these tissues in different conditions, far more complicated than laboratory testing conditions.

To accomplish this aim, the mechanical properties are investigated experimentally and constitutive models are ideated in order to express the stresses experienced by the tissues. These models are then implemented in the numerical simulations. For example, FE models regarding the brain might simulate the impact of the head and quantify the entity of the damage, helping in prevention and treatment. In particular, most of FE simulations for human brain contain a detailed geometrical description of anatomical components, but the mechanical behaviour of the tissue is not accurately described [1].

In this study, soft tissues are simulated by agar gels and the mechanical properties are explored with torsion testing on cylindrical samples of various radius. The goal is the realization of a robust testing protocol for torsion of brain tissue.

The experimental part of this study took place in the National University of Ireland, Galway (NUI Galway).

A brief description of the next chapters is provided. Chapter 1 is about the Traumatic Brain Injury (TBI), a common pathology often underestimated. Researches on the brain tissue might be very helpful for TBI.

In chapter 2, the main concepts of non-linear elasticity are shown, focusing on the constitutive equations for the stresses occurring during large deformations.

Chapter 3 describes the testing methods available for soft tissues. After this overview, the testing technique adopted is extensively explained.

Then, the obtained results are grouped in chapter 4 and chapter 5. In particular, chapter 5 includes the theory of torsion and the estimation of mechanical parameters. In the final part of the chapter, a FE model in Abaqus is illustrated, along with the comparison of experimental and numerical results.

The last chapter contains the statistical analysis of the results.

Chapter 1

Traumatic Brain Injury

The investigation of brain mechanical properties is the key for better understanding a really common type of head injury, the Traumatic Brain Injury (TBI). Accessing strain and strain rates occurring in the brain during impacts allows the prediction of the injury relevance and gives the possibility to develop Finite Element simulations in order to help studying the phenomenon [2].

During an impact, the brain matter undergoes compression, tension and shear [2]. It is proved that the brain bulk modulus is much bigger than the shear modulus, up to 5-6 orders of magnitude: the first is in the order of GPa [3], while the second is in the order of kPa [4][5]. The consequence is that human brain is more sensitive to shear deformations.

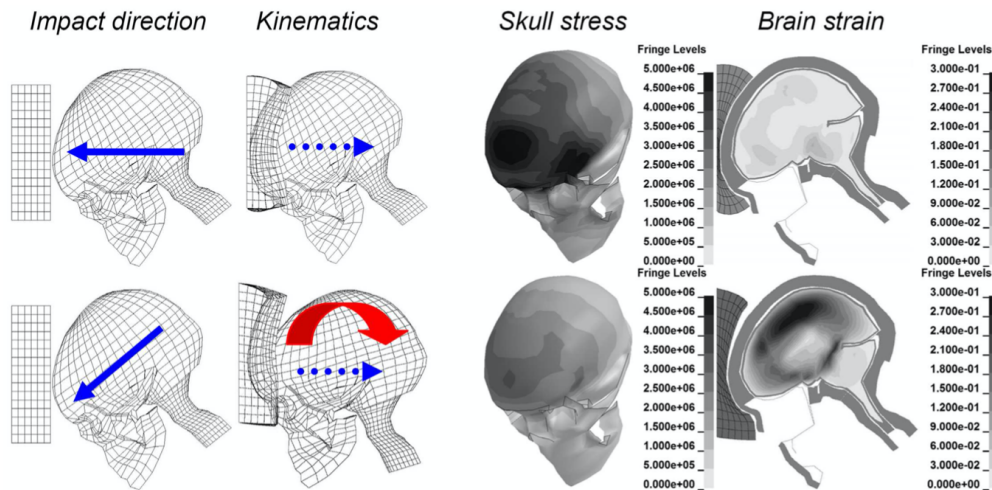


Figure 1.1 – Impact direction, kinematics, skull stress (maximum Von Mises stress for skull bone) and brain strain (maximum Green-Lagrange strain) for radial (upper) and oblique (lower) impact at same collision speed of 6.7 m/s [6].

As demonstrated by Kleiven [7], oblique impacts are more dangerous than radial impacts, talking about Traumatic Brain Injuries: an oblique collision generates both a linear acceleration and a rotational acceleration, instead of the only linear acceleration produced by a pure radial. A rotational kinematics will likely produce a larger shear strain and, therefore, a more severe damage to the brain tissue.

This is clearly visible in figure 1.1: strain in the brain tissue during an oblique impact is much larger than in a radial one, at same collision speed [6]. These levels of strain involve different types of injuries, starting with milder pathologies such as contusions and concussions, up to Diffuse Axonal Injury (DAI) and Subdural Haematoma (SDH). In particular the last two forms of injury are the most severe and can be considered the main cause of death in TBI accidents [6].

On the other hand, figure 1.1 highlights a considerable stress in the skull bone occurring in a radial impact. The main risk in this case is skull fracture [6].

Before going into detail with the TBI, a brief overview on the anatomy of the brain is provided.

1.1 Notions on the brain

The central nervous system (CNS) is composed of *brain* and *spinal cord*. The CNS tissue is organized in grey and white matter: the first is made of cell bodies, dendrites and axon terminals, instead the white matter contains myelin axons, mainly. Other types of cells in the CNS are the glial cells [8].

The CNS is a soft tissue and, consequently, is really delicate. For these reason, it is protected by the cranium, the spinal column, as well as by the meninges (dura mater, arachnoid and pia mater) and by the blood brain barrier. Besides, the cerebrospinal fluid further shields the tissues, absorbing the impacts [8].

The brain, specifically, consists of three main parts (figure 1.2): the forebrain, or prosencephalon, the encephalic trunk and the cerebellum. The forebrain includes the cerebral cortex, responsible for some of the most advanced functions of the brain, such as the control of the motion, the perception, the language, the emotions, the learning mechanisms and the memory. The forebrain also contains thalamus and hypothalamus, that plays an important role in the homeostasis process [8].

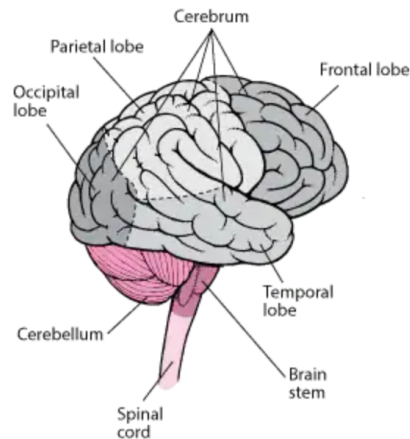


Figure 1.2 – Schematic representation of the brain anatomy [9].

1.2 Traumatic Brain Injury

In the current section, general information about Traumatic Brain Injuries is provided, focusing on the societal impact.

According to Oregon Healthcare [10], "a head injury is a broad term that describes a vast array of injuries that occur to the scalp, skull, brain and underlying tissue and blood vessels in the head; head injuries are also commonly referred to as brain injury, or traumatic brain injury (TBI), depending on the extent of the head trauma".

Approaching TBI, the first issue faced is the definition of the injury: different authors adopt different ways of describing this pathology, triggering confusion and preventing a clear understanding of the epidemiology [10]. Generally speaking, TBI is a form of injury occurring to the brain (not related to degenerative or congenital problems) and caused by an external loading, heading to non-physiological, cognitive or behavioural dysfunction [11]. The "Centers for Disease Control and Prevention" (CDC) defines TBI as "an occurrence of injury to the head that is documented in a medical record with one of the following conditions attributed to head injury: (1) observed or self-reported decreased level of consciousness, (2) amnesia, (3) skull fracture, or (4) objective neurological or neuropsychological abnormality or diagnosed intracranial lesion" [12]. Another definition of TBI comes from the American "Department of Veterans Affairs and Department of Defense" (VA/DoD) [13] which states that TBI is "a traumatically induced structural injury and/or physiological disruption of brain function as a result of an external force that is indicated by new onset or worsening of at least one of the following clinical signs, immediately following the event:

- any period of loss of or decreased level of consciousness;
- any loss of memory for events immediately before or after the injury;
- any alteration in mental state at the time of the injury (confusion, disorientation, slowed thinking, etc.);
- neurological deficits (weakness, loss of balance, change in vision, praxis, paresis/plegia, sensory loss, aphasia, etc.) that may or may not be transient;
- intracranial lesion."

The abundance of definitions is due to a non-universal method to assess TBI because every criterion is based on the operator or examiner opinion [14].

1.2.1 Classification and symptoms

TBI involves physical, emotional and cognitive impairments, with possible loss of consciousness (LOC) [14]. Typical symptoms, as indicated by the "American Academy of Neurology" (AAN) [15], are amnesia, behaviour or personality changes, delayed verbal and motor responses, disequilibrium, disorientation, incoherent speech and vacant stare. Nausea, vomiting, headache and sleeping disorders are also common signs of head trauma. Duration of symptoms varies among subjects and depending on the severity of the trauma, ranging from minutes to several months [14].

Based on the duration and on the entity of symptoms, numerous classification scales have been ideated, trying to reach a uniformity of evaluation. Moreover a correct classification of the injury allows the prediction of short and long-term consequences [11].

The most used method to determine TBI severity is the "Glasgow Coma Scale" (GCS): it tests the consciousness of the subject, by giving eye opening, verbalization and motor response stimuli and marking his/her responsiveness with a number from 3 (the patient does not produce an answer) to 15 (the subject is fully responsive) [11]. Usually GCS values from 13 to 15 correspond to mild TBI, from 9 to 12 to moderate TBI and lower values represent a subject with severe TBI.

Another common classification method is based on "Post-traumatic amnesia" (PTA), a state in which the person is conscious, but presents confusion, disorientation and poor attention [11]. One of the first classification system based on this concept has been proposed by Russell and Smith in 1961 [16]: the patient suffers a mild injury if PTA lasts 1 hour or less, moderate injury if PTA ranges from 1 to 24 hours and severe injury up to 7 days (Table 1.1).

	Mild	Moderate	Severe	Very severe
Glasgow coma scale	13-15	9-12	6-8	3-5
Russell posttraumatic amnesia	<1 h	1–24 h	1–7 days	>7 days

Table 1.1 – Injury classifiers.

Presented indicators show some defects: for instance, GCS is an accurate predictor of mortality and morbidity, but tends to overestimate the seriousness of the injury if evaluated too close to the impact, in aphasic patients, subjects who took alcohol or drugs or simply with facial impairments. On the other hand, Russell PTA is reliable as long-term predictor (e.g. return to work), but not usable immediately after the accident because the subject needs to exit the confusion state. Moreover, these classifiers are particularly useful when facing moderate and severe TBIs, but have some problems with mild TBI because of the great mutability of phenomenon expressions. Therefore, subjects with the same score, derived from GCS or PTA, might result in different long-term conditions [11].

A common term related to TBI is *concussion*: as established by the "Centers for Disease Control and Prevention" (CDC) and by the "World Health Organization" (WHO), concussion can be intended as a synonym of mild TBI [14]. The most respected and cited definition of mild TBI has been formulated by the "American Congress of Rehabilitation Medicine" (ACRM) in 1993 [17] and states that "a patient with mild traumatic brain injury is a person who has had a traumatically induced physiological disruption of brain function, as manifested by at least one of the following: (1) any period of loss of consciousness, (2) any loss of memory for events immediately before or after the accident, (3) any alteration in mental state at the time of the accident (e.g. feeling dazed, disoriented, or confused), and (4) focal neurological deficit(s) that may or may not be transient; but where the severity of the injury does not exceed the following:

- loss of consciousness of approximately 30 minutes or less;
- after 30 minutes, an initial Glasgow Coma Scale (GCS) of 13-15;
- post-traumatic amnesia (PTA) not greater than 24 hours."

Consequently, a concussion might be thought as a neurocognitive or behavioural impairment caused by biomechanical forces transmitted to the brain, with usually no structural changes visible from the outside [18]. From a biochemical point of view, these forces damage cellular membranes, promoting transient membrane faults and ionic flux. This is the starting point of a metabolic cascade that takes to a energy shortage and cerebral blood flow decrease, resulting in metabolic worsening [18].

There is still a lack of knowledge about mild TBI, with lots of researchers dealing with it in order to find thresholds suitable for most people [18].

Another type of classification can be made based on the *lesion entity*. Then, the injury might be focal or diffuse [19]. Among focal lesions, primary vascular injuries are the most important and consist in bleeding within the brain or on the surface of the brain. Vascular injuries belong to moderate and severe category[19]; Acute Subdural Haematoma (SDH) is an example of this type of injury and is one of the most severe TBI, responsible for a large part of deaths [6]. The main process provoking SDH is the tearing of veins [6], and Gennarelli found that this was produced by angular acceleration of the head and by relative motion between skull and brain [20].

Diffuse lesions are not contained in a limited region of the brain, but in a larger part of the organ. Among these lesions, the most common is the Diffuse Axonal Injury (DAI), a severe TBI that is responsible, together with SDH, for more deaths than any other TBI type [6]. The mechanism accountable for DAI is a massive rotational acceleration of the brain, causing shear, compression and tensile strain of the tissue. When the human brain undergoes a rapid rotation, the brain tissue loses its elastic properties, becoming more delicate and susceptible to "break". The axonal cytoskeleton suffers a structural harm, resulting in a disruption of the axonal network and, therefore, in an extended injury. Because of the viscoelastic response of the axons, the axonal injury is dependent on both the magnitude of strain and the strain rate during a trauma [21]. Several groups investigated threshold values for strain and strain rate, finding 10-50% of shear strain and 10-50 Hz as strain rate [2].

1.2.2 Causes, incidence on population and socio-economic impact

According to a statistical survey conducted by the "Centers for Disease Control and Prevention" (CDC) from 2002 to 2006 [22], TBI causes in the United States are divided as follows (combining Emergency Department visits, hospitalizations and deaths):

- falls (35.2%);
- motor vehicle-related injuries (17.3%);
- struck by/against events, which include colliding with a moving or stationary object (16.5%);
- assaults (10%);
- other or unknown causes (21%).

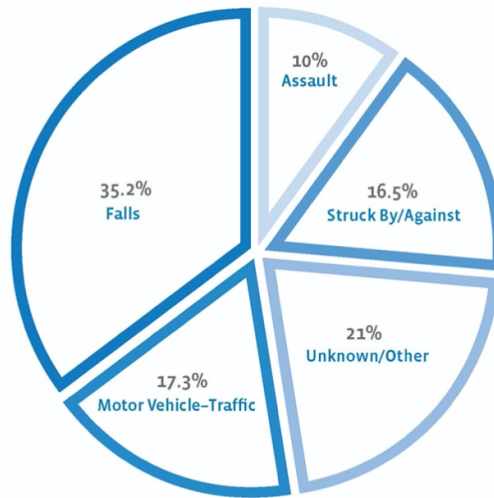


Figure 1.3 – Estimated percentage of TBI causes in USA from 2002 to 2006 [22].

Figure 1.4 clearly shows that falls are more common in children and elderly people over 65, while motor vehicle accidents usually involve late adolescents or young adults from 15 to 30.

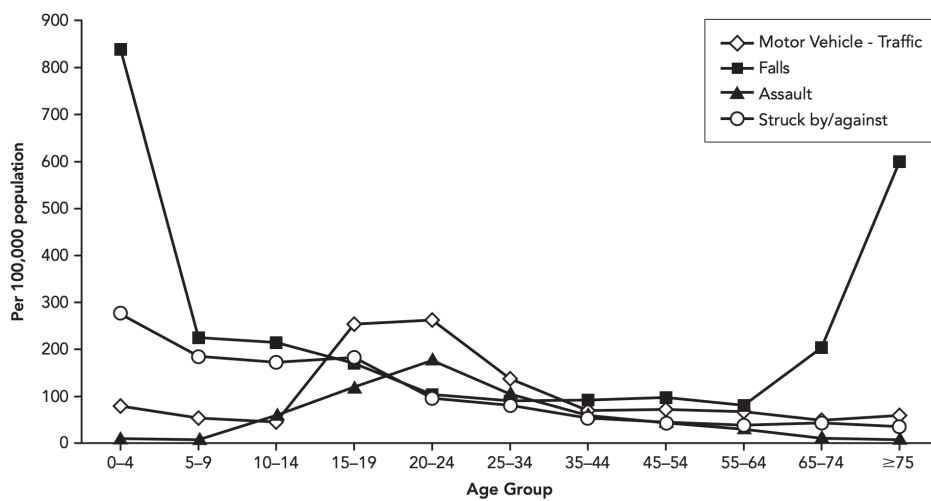


Figure 1.4 – Annual rate of TBI related with age groups [23].

More generally, children under 4 and adolescents from 15 to 19 are the most affected categories and are responsible for most Emergency Department visits, while adults over 75 have the highest rates of hospitalization and death [22]. In the same period, mild TBIs result in 75% of total cases, moderate TBIs in 22% and severe TBIs in 3% [19].

The same CDC survey cited above [22] estimates 1,691,481 people experiencing a form of TBI annually in the United States. This total is composed of: 1,364,797 subjects (approximately 80%) visiting Emergency Department, 275,146 hospitalizations and 51,538 deaths, contributing to 30.5% of all injury-related deaths. Emergency Department visits and hospitalizations grew over the years, but this might be due to the population increasing and to better knowledge about the injury. On the other hand, deaths slightly fell, probably because of the improvement in safety measures and treatments [11].

Another issue is the birth of new disabilities related to TBI: during the year 2003 in the United States, Selassie et al. conducted a research about long-term disability among hospitalized TBI survivors and found out that 124,626 out of 288,009 subjects (43.3%) developed a form of disability [24]. A research study by Zaloshnja et al. showed that, in 2005, 3.17 million people or 1.1% of the United States civilian population suffered from long-term disability due to TBIs [25]. A CDC survey stated that, in 1996, individuals with disability were even 5.3 million [26].

Moreover, the numbers of TBI cases is certainly underestimated, mainly because of injured people who do not ask for medical care or have been treated in outpatient settings, without ED visits, so that cannot be included in statistical surveys [14]. This is common in sport accidents [11].

These huge numbers are responsible for the economic and societal impact of TBI: medical costs, lost productivity and loss of quality life amount to 60 billion dollars annually in the USA according to a study for the year 2000, or 221 billion if compared with 2009 dollars [11]. It has been estimated that with a 25% decrease of TBI related accidents, 25 billion dollars would be saved [6].

But the TBI burden is not over: consequences on the individual life are widespread. Usually the injured subject, who face long-term disability, has problems with reintegration in social life, such as school, job or community activities. Unemployment could also be challenging: researchers stated that one out of five hospitalized TBI survivors has not returned to work after one year from the injury [11]. Their interpersonal relationships might be influenced, especially with young adults, tracing the path for social isolation [11].

Research on head trauma is essential in order to improve prevention systems and consciousness of the topic. Really active fields are sports and vehicular safety.

Chapter 2

Nonlinear Elasticity

The birth of Nonlinear Elasticity corresponds to the need of modelling the mechanical behaviour of rubber undergoing large deformations. This discipline develops in 1950s thanks to the work of Ronald Rivlin. From 1980s these concepts are applied to the modelling of biological soft tissues such as skin, arterial wall, cardiac muscle, brain, tumours or tendons. The aim is to provide accurate simulations for applications in mechanical engineering and bio-engineering.

Elasticity is easy to understand: if you apply external forces to an elastic body, it deforms immediately. When the force is removed, it returns to original size and shape instantaneously.

Elasticity can be considered an idealization of reality: it is suitable for small deformations of many materials, such as metals or glass, but cannot model lots of real-world applications, including several biomaterials and real tissues used in bioengineering and biomedicine, as they undergo large deformations [27].

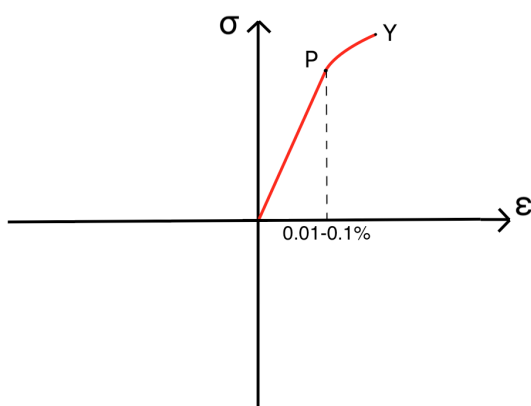


Figure 2.1 – Typical stress-strain response curve in tensile tests of a metal [27].

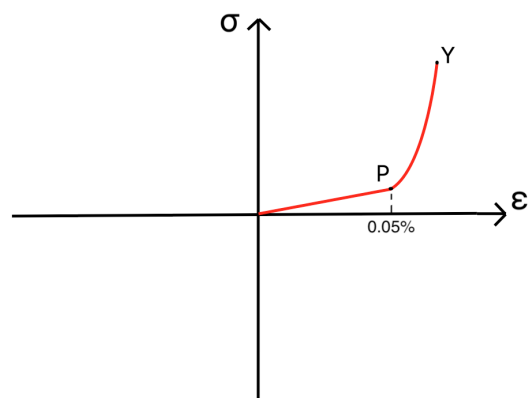


Figure 2.2 – Typical stress-strain response curve in tensile tests of a soft tissue [27].

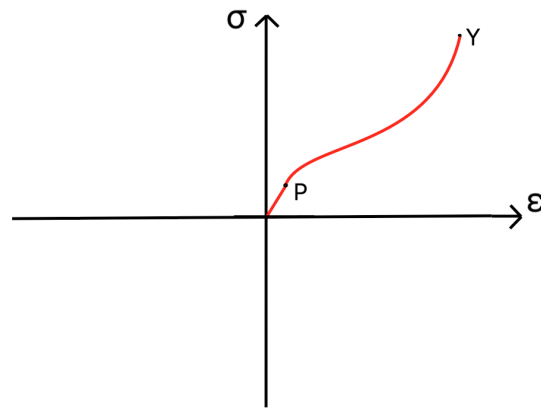


Figure 2.3 – Typical stress-strain response curve in tensile tests of a rubber [27].

Linear elasticity involves the mechanics of solids for which the stress σ is proportional to the strain ϵ in a certain type of test.

Figure 2.1 shows a typical response curve for a metal. The point P is the limit of proportionality and Y is the yield point, that is beyond Y the body undergoes plastic deformation, not returning to its original shape and state once the load is removed. Usually, P corresponds to a strain in the 0.01%–0.1% range. Therefore, the linear theory can be employed for the stress σ with respect to the strain ϵ . This is the foundation of the *infinitesimal*, or classical, theory of elasticity [27].

Figure 2.2 shows a typical tensile response for a biological soft tissue. The point Y corresponds to a strain region of 10%–100%. The P–Y part of the curve corresponds to the “strain-stiffening” effect. The regime O–P is larger than for metals, reaching 5% strain. In this case, linearisation in terms of ϵ is not appropriate, as the strains are *finite* [27].

Figure 2.3 shows a typical tensile response for rubber-like materials. Rubbers and elastomers extend up to 100%–500% of their initial length. Linear elasticity can be used only for the very first part of the curve [27].

The initial slope of the tensile tests plots gives a measure of the initial stiffness of a given solid. For instance, the slope for steel is at least 1000 times steeper than the initial slope for rubber, and 100 times steeper than the initial slope for tendons (one of the stiffest biological soft tissue, made of more than 80% collagen in mass). This is why rubbers and tissues are often called “soft” solids [27].

These different behaviours can be explained by different *microscopic structures*. Thus, a typical metal has an atomic lattice structure and only short-range movements are allowed. Rubber-like materials are made up of long chain molecules, which are spread randomly and can move quite freely. Biological soft tissues are essentially made of an elastin matrix with embedded collagen fibres. In particular, collagen is three orders of magnitude stiffer than elastin and the contribution of these fibres is felt in the strain-stiffening part of the curve [28].

The following sections will focus on introducing the main concepts of Continuum Mechanics, necessary for modelling the behaviour of the brain under large deformations.

2.1 Kinematics

2.1.1 Bodies, configurations and motions

A *body* \mathcal{B} is a continuous set whose elements can be put into one-to-one correspondence with points of a region B in a three-dimensional Euclidean point space. The elements of \mathcal{B} are called *particles* (or *material points*) and B is called a *configuration* of \mathcal{B} .

As the body moves, the configuration changes with time. Let $t \in I \subset \mathbb{R}$ denote time, where I is an interval in \mathbb{R} . If, with each $t \in I$, a unique configuration B_t of \mathcal{B} (referred as *current configuration*) is associated, then the family of configurations $\{B_t : t \in I\}$ is called a *motion* of \mathcal{B} . It is assumed that as \mathcal{B} moves continuously then B_t changes continuously.

It is convenient to identify a *reference configuration*, B_r , which is an arbitrarily chosen fixed configuration. Then, any particle P of the body \mathcal{B} may be labelled by its position vector \mathbf{X} in B_r relative to some origin O . Let \mathbf{x} be the position vector of P in the configuration B_t at time t relative to an origin o (which need not coincide with O), as shown in figure 2.4.

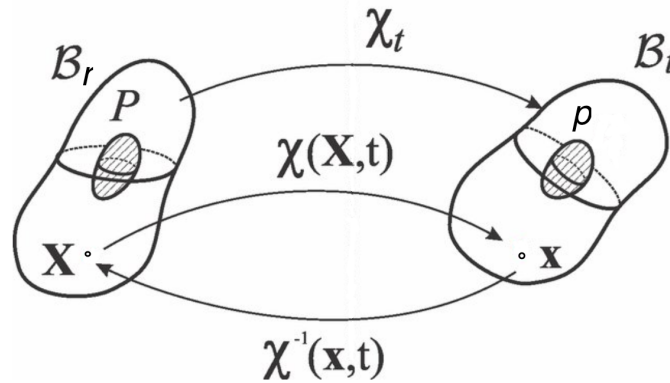


Figure 2.4 – Reference configuration B_r and current configuration B_t with position vectors \mathbf{X} and \mathbf{x} of a material point P [29].

The body \mathcal{B} occupies the configuration B_t at time t . Besides, B_r does not require to be a configuration actually occupied by \mathcal{B} during the motion, but it is often chosen to be the configuration occupied by \mathcal{B} at the initial time.

Since B_r and B_t are configurations of \mathcal{B} , there exists a bijection mapping $\chi : B_r \rightarrow B_t$ such that (as depicted in figure 2.4)

$$\begin{aligned} \mathbf{x} &= \chi(\mathbf{X}) \quad \text{for all } \mathbf{X} \in B_r, \\ \mathbf{X} &= \chi^{-1}(\mathbf{x}) \quad \text{for all } \mathbf{x} \in B_t. \end{aligned} \tag{2.1}$$

The mapping χ is called the *deformation* of the body from B_r to B_t . Since B_t depends on t , the correct formulation is:

$$\mathbf{x} = \chi(\mathbf{X}, t) \quad \text{for all } \mathbf{X} \in B_r, t \in I. \tag{2.2}$$

For each particle P (with label \mathbf{X}) this describes the motion of P with t as parameter, and hence the motion of the whole body \mathcal{B} .

In the case of B_r , the position vector \mathbf{X} and time t serve as independent variables, and the fields are then said to be defined in terms of the *referential* or *material* description. Alternatively, in the case of B_t , \mathbf{x} and t are used and the description is said to be *spatial*. The terminologies *Lagrangian* and *Eulerian descriptions* are also used in respect of B_r and B_t .

Rectangular Cartesian coordinate systems with basis vectors $\{ \mathbf{E}_i \}$ and $\{ \mathbf{e}_i \}$ are chosen for B_r and B_t respectively, with *material coordinates* X_i and *spatial coordinates* x_i ($i = 1, 2, 3$). Thus, relative to the origins O and o respectively, we have:

$$\mathbf{X} = X_i \mathbf{E}_i, \quad \mathbf{x} = x_i \mathbf{e}_i. \tag{2.3}$$

2.1.2 Deformation Gradient

Let Grad and grad denote the gradient operator in the reference configuration (with respect to \mathbf{X}) and in the current configuration (with respect to \mathbf{x}), respectively.

Then, the *deformation gradient tensor* \mathbf{F} is defined as:

$$\mathbf{F}(\mathbf{X}, t) = \text{Grad} \mathbf{x} \equiv \text{Grad} \chi(\mathbf{X}, t). \tag{2.4}$$

And reminding the definition of gradient of a vector, it is possible to write with respect to the chosen basis vector

$$F_{ij} = \frac{\partial x_i}{\partial X_j}, \tag{2.5}$$

with $x_i = \chi_i(\mathbf{X}, t)$.

From (2.5), results

$$d\mathbf{x} = \mathbf{F}d\mathbf{X}, \tag{2.6}$$

$$d\mathbf{X} = \mathbf{F}^{-1}d\mathbf{x}. \tag{2.7}$$

Equation (2.7) is true if $\det F \neq 0$, so that F has an inverse.

Using the "polar decomposition theorem" for the deformation gradient F , the following tensor measures of deformation can be obtained:

$$C = F^T F = U^2, \quad B = F F^T = V^2, \quad (2.8)$$

with U and V positive definite, symmetric tensors called *right and left stretch tensors*. C and B are known as the *right and left Cauchy-Green deformation tensors* respectively.

2.1.3 Deformation of line, area and volume elements

Equation (2.6) describes how infinitesimal *line elements* dX of material at X transform under the deformation into dx (which consists of the same material as dX) at x . It shows that locally, *line elements* transform *linearly* since F depends on X (and not on dX). Thus, at each X , F is a *linear mapping* (i.e. a second-order tensor).

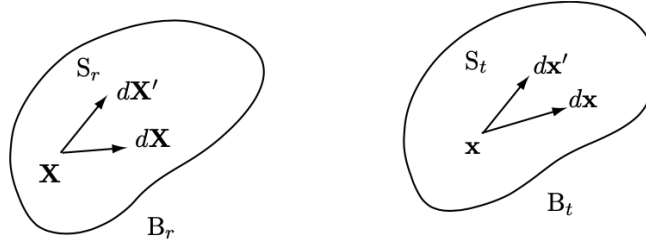


Figure 2.5 – Infinitesimal line elements at X on the surface S_r in the reference configuration B_r and their images at x on the deformed surface S_t in the current configuration B_t .

The change in volume is defined as follows:

$$dv = JdV, \quad \text{where } J = \det F. \quad (2.9)$$

Equation (2.9) shows that J is a measure of the *change in volume* under the deformation. If the deformation is such that there is no change in volume then the deformation is said to be *isochoric*. In that case:

$$J = \det F = 1. \quad (2.10)$$

Equation (2.10) is a good approximation in many cases and is adopted as an idealization. An ideal material for which (2.10) holds for all deformations is called an *incompressible material*.

Regarding surface elements, equation (2.11), known as Nanson's formula, explains how elements of *surface area* deform:

$$nda = JF^{-T}NdA, \quad (2.11)$$

with dA and da surface area elements on S_r and S_t respectively (see figure 2.5), and N and n unit normals at X and x respectively.

2.1.4 Measures of strain

Strain is measured locally by changes in the lengths of line elements. In other words, "strain measures the changes in distance of two particles, one at position X , the other at position $X + dX$, in the reference configuration, mapped into positions x and $x + dx$ in the current configuration" [27].

Several definitions of strain exist, including:

- *Green strain tensor* E , or *Lagrangian strain tensor*, measuring the change in the squared length of a line element

$$E = \frac{1}{2}(F^T F - I) = \frac{1}{2}(C - I) = \frac{1}{2}(U^2 - I); \quad (2.12)$$

- *Eulerian strain tensor* e , the equivalent of E with respect to the spatial line elements

$$e = \frac{1}{2}(I - (F^{-1})^T F^{-1}) = \frac{1}{2}(I - B^{-1}) = \frac{1}{2}(I - V^{-2}). \quad (2.13)$$

2.2 Balance laws and governing equations of motion

The mechanics of continuous media is characterised by equations which represent the balance of mass, linear momentum, angular momentum and energy in a moving body. These balance equations concern all bodies, solid or fluid, and each produces field equations (differential equations for scalar, vector and tensor fields).

2.2.1 Mass conservation

Let R_t be an arbitrary material region in the current configuration B_t . Its mass can be written as

$$m = \int_{R_t} \rho dv. \quad (2.14)$$

where ρ is the (current) *mass density per unit volume*. As R_t moves it always consists of the same material, so its mass does not change and, after some calculation, the *conservation of mass equation* (or *continuity equation*) is found:

$$\dot{\rho} + \rho \operatorname{div} v = 0. \quad (2.15)$$

Specifically, $\operatorname{div} v$, where v is the deformation velocity, measures the rate at which volume changes during the motion.

2.2.2 Balance of linear and angular momentum

Starting from the *Euler's laws of motion*

$$\frac{dM}{dt} = F, \quad \frac{dH}{dt} = G, \quad (2.16)$$

(where M and H are the *linear* and *angular momentum* respectively and F and G are the *total forces* and *moments* respectively), it is possible to obtain the formulation for the linear and angular momentum balance.

More precisely, the total forces acting on a body are represented as the sum of *body* and *contact forces*:

- body forces can be expressed as

$$\int_{R_t} \rho \mathbf{b} dv, \quad (2.17)$$

where \mathbf{b} are the body forces *per unit mass*;

- contact forces acting on the boundary ∂R_t of R_t can be expressed as

$$\int_{\partial R_t} \mathbf{t}_{(n)} da, \quad (2.18)$$

where $\mathbf{t}_{(n)}$ is referred as the *stress vector* and \mathbf{n} is the unit outward normal to S (as depicted in figure 2.6).

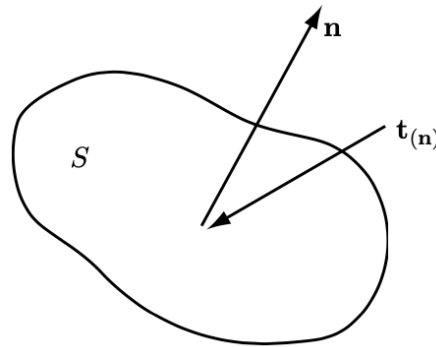


Figure 2.6 – Stress vector $\mathbf{t}_{(n)}$ at a point of the surface S where the unit normal is \mathbf{n} .

On the other hand, total moments acting on a body can be described as the sum of *body* and *contact moments*:

- body moments can be expressed as

$$\int_{R_t} [\mathbf{x} \times (\rho \mathbf{b}) + \rho \mathbf{c}] dv, \quad (2.19)$$

where \mathbf{c} are the body moments *per unit mass*;

- contact, or surface, moments acting on the boundary ∂R_t of R_t can be expressed as

$$\int_{\partial R_t} \mathbf{x} \times \mathbf{t}_{(n)} da. \quad (2.20)$$

Now, setting body torques to zero (i.e. $\mathbf{c} = 0$), linear and angular momentum balance, respectively, are obtained:

$$\frac{d\mathbf{M}}{dt} = \frac{d}{dt} \int_{R_t} \rho \mathbf{v} dv = \int_{R_t} \rho \mathbf{b} dv + \int_{\partial R_t} \mathbf{t}_{(n)} da, \quad (2.21)$$

$$\frac{d\mathbf{H}}{dt} = \frac{d}{dt} \int_{R_t} \rho \mathbf{x} \times \mathbf{v} dv = \int_{R_t} \rho \mathbf{x} \times \mathbf{b} dv + \int_{\partial R_t} \mathbf{x} \times \mathbf{t}_{(n)} da. \quad (2.22)$$

2.2.3 Cauchy's theorem

"Let $(\mathbf{t}_{(n)}, \mathbf{b})$ be a system of contact and body forces for \mathcal{B} during a motion. A necessary and sufficient condition for the momentum balance equations (2.21) and (2.22) to be satisfied is that there exists a second-order tensor $\boldsymbol{\sigma}$, called the *Cauchy stress tensor*" [27], such that

- (i) for each unit vector \mathbf{n} ,

$$\mathbf{t}_{(n)} = \boldsymbol{\sigma}^T \mathbf{n}, \quad (2.23)$$

where $\boldsymbol{\sigma}$ is independent of \mathbf{n} ,

- (ii)

$$\boldsymbol{\sigma}^T = \boldsymbol{\sigma}, \quad (2.24)$$

- (iii) $\boldsymbol{\sigma}$ satisfies the *equation of motion*

$$\operatorname{div} \boldsymbol{\sigma} + \rho \mathbf{b} = \rho \mathbf{a}. \quad (2.25)$$

where $\mathbf{a} \equiv \dot{\mathbf{v}}$ is the acceleration.

The proof of Cauchy's theorem is omitted. Main consequences are: linearity of the surface traction $\mathbf{t}_{(n)}$ is linear in \mathbf{n} (2.23); the equation of motion (2.25) represents the local form of the equation of balance of *linear* momentum, while the symmetry of the Cauchy's stress tensor σ (2.24) guarantees the global and local balance of *angular* momentum.

Other formulations for stress tensors commonly used are:

- the *nominal stress tensor* S measures the force *per unit reference area* (while σ measures the force *per unit deformed area*) and is defined as

$$S = JF^{-1}\sigma; \quad (2.26)$$

- the *first Piola-Kirchhoff stress tensor*, defined as

$$P \equiv S^T = J\sigma(F^{-1})^T. \quad (2.27)$$

Normal and shear stresses

Let consider an element of area da on a surface S with unit normal \mathbf{n} , subjected to a contact force $\mathbf{t}_{(n)}da$. The *normal component* of the stress vector, denoted σ , is defined as

$$\sigma = \mathbf{n} \cdot \mathbf{t}_{(n)} = \mathbf{n} \cdot (\sigma\mathbf{n}). \quad (2.28)$$

This is called the *normal stress* on the surface S . It is tensile when positive and compressive when negative.

The stress vector tangential to S , called *shear stress*, is denoted τ , with magnitude τ , and given by

$$\boldsymbol{\tau} \equiv \mathbf{t}_{(n)} - \sigma\mathbf{n}, \quad \tau = |\mathbf{t}_{(n)} - \sigma\mathbf{n}|. \quad (2.29)$$

2.3 Constitutive equations

The following equations governing the motion of a continuous body have been determined: equation of *mass conservation* (2.15), equation of *motion* (2.25) and equation of *angular momentum balance* (2.24).

So, 7 out of 13 (i.e. ρ , v (3 components) and σ (9 components)) scalar fields are found out thanks to these equations. The *constitutive equations* provide the remaining 6 components of σ in terms of kinematical quantities.

The focus will be on *homogeneous elastic materials*, where σ depends on F only. These types of material are also called *Cauchy elastic*. In particular, *Green elasticity*, or *hyperelasticity*, will be treated, for which the stress is derived from a *strain energy function* W , which depends on F only: $W = W(F)$ [27].

Consequently the *nominal* and *Cauchy* stresses can be rewritten with respect to the *strain energy function*, or *elastic stored energy*, $W(\mathbf{F})$ per unit volume in the reference configuration B_r :

$$\mathbf{S} = \frac{\partial W}{\partial \mathbf{F}}, \quad (2.30)$$

$$\boldsymbol{\sigma} = J^{-1} \mathbf{F} \frac{\partial W}{\partial \mathbf{F}}. \quad (2.31)$$

$W(\mathbf{F})$ represents the work done (per unit volume at \mathbf{X}) by the stress in deforming the material from B_r to B_t (i.e. from \mathbf{I} to \mathbf{F}) and is independent of the path taken in deformation space.

2.3.1 Isotropic hyperelasticity

"A material is said to be *isotropic* relative to B_r , when its mechanical behaviour is unaffected by any rotation \mathbf{P} that takes place prior to a given deformation. Physically, this means that the response of a small specimen of material cut from B_r is independent of its orientation in B_r " [27]. Mathematically, this can be expressed with the following equation:

$$W(\mathbf{F}) = W(\bar{\mathbf{F}}) = W(\mathbf{F}\mathbf{P}^T). \quad (2.32)$$

Moreover, for an *isotropic hyperelastic material* the strain energy function may be written as

$$W(\mathbf{F}) \equiv W(I_1, I_2, I_3), \quad (2.33)$$

highlighting its dependence on the principal invariants only.

Therefore, the nominal stress \mathbf{S} is related to W through

$$\mathbf{S} = \sum_{i=1}^3 \frac{\partial W}{\partial I_i} \frac{\partial I_i}{\partial \mathbf{F}}. \quad (2.34)$$

2.3.2 Incompressible elastic materials

Incompressible materials can only undergo *isochoric* deformations. The deformation gradient \mathbf{F} must satisfy the internal constraint

$$J \equiv \det \mathbf{F} = 1. \quad (2.35)$$

Besides the third invariant is equal to 1 ($I_3 = 1$).

In conclusion, the general stress-strain relationships for *incompressible isotropic hyperelastic* materials are:

- Cauchy stress

$$\boldsymbol{\sigma} = -p\mathbf{I} + 2\frac{\partial W}{\partial I_1}\mathbf{B} - 2\frac{\partial W}{\partial I_2}\mathbf{B}^{-1}, \quad (2.36)$$

- nominal stress

$$\mathbf{S} = -p\mathbf{F}^{-1} + 2\frac{\partial W}{\partial I_1}\mathbf{F}^T - 2\frac{\partial W}{\partial I_2}\mathbf{F}^{-1}\mathbf{B}^{-1}, \quad (2.37)$$

where p is a Lagrange multiplier, which will be eliminated/determined from the equations of motion/equilibrium and the boundary/initial conditions, and \mathbf{B} is the left Cauchy-Green strain tensor.

2.3.3 Examples of strain energy functions

Many different strain energy functions are available in the literature to model the behaviour of rubber like solids and other soft materials, including:

- *neo-Hookean* material

$$W = \frac{\mu_0}{2}(I_1 - 3), \quad (2.38)$$

where μ_0 is the *shear modulus* of the material and substituting in (2.36)

$$\boldsymbol{\sigma} = -p\mathbf{I} + \mu_0\mathbf{B}; \quad (2.39)$$

- *Mooney-Rivlin* material

$$W = C_1(I_1 - 3) + C_2(I_2 - 3), \quad (2.40)$$

where C_1 and C_2 are constants and substituting in (2.36)

$$\boldsymbol{\sigma} = -p\mathbf{I} + 2C_1\mathbf{B} - 2C_2\mathbf{B}^{-1}; \quad (2.41)$$

- *Gent* model

$$W = -\frac{\mu_0 J_m}{2} \ln\left(1 - \frac{I_1 - 3}{J_m}\right), \quad (2.42)$$

where μ_0 and J_m are positive constants and substituting in (2.36)

$$\boldsymbol{\sigma} = -p\mathbf{I} + \frac{\mu_0 J_m}{J_m + 3 - I_1}\mathbf{B}; \quad (2.43)$$

- *Fung* material

$$W = \frac{\mu_0}{2b} e^{b(I_1 - 3)}, \quad (2.44)$$

where μ_0 and b are positive constants and substituting in (2.36)

$$\boldsymbol{\sigma} = -p\mathbf{I} + \mu_0 e^{b(I_1 - 3)}\mathbf{B}. \quad (2.45)$$

After the choice of the strain energy function, by using the formulation of σ , it is possible to predict how a material reacts to applied forces. Then, the model is compared to collected experimental data, in order to evaluate its goodness. The parameters presented in the mentioned models are adjusted in order to get a closer fit between experimental and theoretical curves.

Chapter 3

Materials and methods

Soft tissues and, in particular, brain matter are really difficult to test, due to their brittleness and fragility [4]. Despite of decades of research on animal and human brain, an accurate mechanical characterization is still unavailable [30]. The wide choice among testing methods and the complexity of the tissue contribute to large differences in the literature reported values of bulk and shear moduli [19], reaching three orders of magnitude difference for bulk modulus in computational head models of brain biomechanics [3]. The same for viscoelastic response, with considerable variance in reported values of storage modulus (G') and loss modulus (G'') [1].

The first aspect to consider is the difference in the used material: lots of studies use animal brains, such as sheep or porcine, for the easier availability and a minimum post-mortem time. Moreover, they turn out to be reliable substitutes for human brains, with small differences in the mechanical properties. Testing conditions are another important issue to deal with: in particular temperature, glueing, anisotropy of the material and preparation of the tissue might largely influence the stiffness [1].

3.1 Brain mechanical testing techniques

The main distinction is between *in vitro* and *in vivo* methods.

The latter is a more recent approach, conducted on healthy animal and human subjects for the purpose of getting more realistic data. Among *in vivo* methods, *magnetic resonance elastography* (MRE) is the most widespread, able to measure dynamic properties of a soft tissue in a non-invasive way. The idea is to provide a mechanical excitation and detect the wave propagation through a magnetic resonance imaging device, as depicted in figure 3.1 [30].

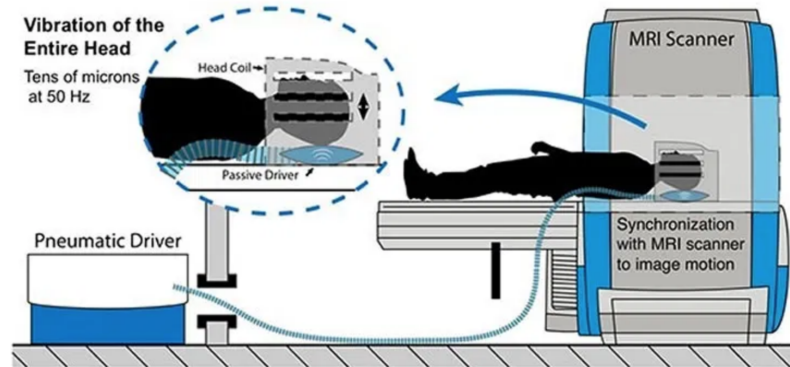


Figure 3.1 – MRE testing representation [31].

Moving on to *in vitro* methods, different techniques are adopted by various research groups. Usually these types of tests are *destructive*, so the samples are used only once. The *torsion test*, employed in this study, will prove to be an excellent solution.

A common procedure is the *tensile test*, realised with cylindrical samples glued to the tension plates (figure 3.2). As pointed out by Rashid et al., the fixed attachment produced by the glue creates a "strongly inhomogeneous deformation field" in the region of the sample closed to the surfaces, generating unreal stress–strain curves [32].

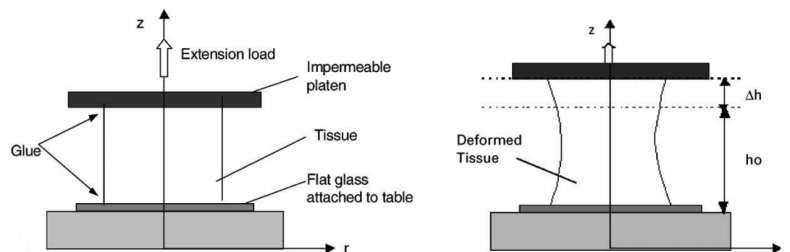


Figure 3.2 – Sketch of the experimental set-up suitable for tension tests of soft tissues [33].

Another typical procedure is the *compression test*: the experimental set-up is similar to the tensile test. A homogeneous deformation is achievable through the lubrication of the plates, but only with a small amount of strain (about 10%), before the bulging of the tested tissue [4].

A further test is the *simple shear test*, in which the sample is glued between two parallel plates, one fixed and the other mobile. The mobile plate moves horizontally producing a homogeneous deformation, as shown in figure 3.3. As demonstrated by Destrade et al., simple shear experiments reach up to 60% strain

with porcine brain matter, managing to model the tissue through the Mooney-Rivlin strain energy function [34]. The 60% strain limit, additionally, enables this type of test to be appropriate for the study of the diffuse axonal injury (DAI), often associated with TBI [34].

Lastly, *torsion tests* represent a good alternative to simple shear, when talking about soft tissues. Torsion can be implemented by glueing a cylindrical sample between two parallel plates and then rotating one of them. The experiment is possible by means of a particular machine, called *rheometer* [4].

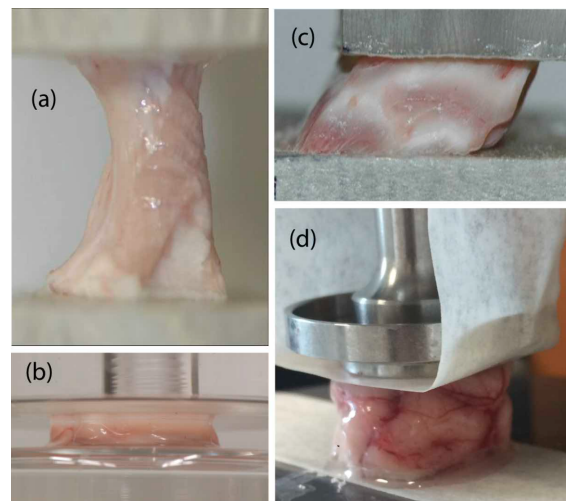


Figure 3.3 – Standard testing protocols for soft solids applied to brain matter: (a) tensile, (b) compression, (c) simple shear and (d) torsion tests [4].

Another advantage of simple shear and torsion tests is the possibility to visualize a typical non-linear phenomenon occurring in soft solids, called the *Poynting effect*. This phenomenon describes the tendency of the sample to expand (positive Poynting effect) or contract (negative Poynting effect) in the direction normal to the plates when the sample is sheared or twisted [4]. In other words, it is possible to record a perpendicular force acting on the plates. The effects on the brain is not negligible at all: as a matter of fact, Balbi et al. highlighted that these type of forces are responsible for "high normal stresses developing during rotational impacts" and might be cause of TBI in the subject [4].

Concerning Poynting effect, torsion tests are preferable because rheometers allow to measure normal forces on the plates (through built-in load cells), by contrast to current simple shear devices [4]. Therefore, torsion is an optimal testing method, making possible the evaluation of two sets of data: the *torque* and the *normal force*, as explained in the next section.

3.2 Testing procedure

In this section, the testing procedure, consisting of materials, equipment, experimental set-up and protocol, is illustrated.

3.2.1 Agar gels

Agar gel samples are tested in this study. Agar gels are composed of agarose, a natural polysaccharide with great gelling capacity. Gels are massively used by researchers in order to simulate biological soft tissues during experiments, as they bring several benefits. Firstly, they are obviously easier to produce in large quantities and are simple to handle. Gels might be used for the "exploration and calibration stages of the experimental research", paving the way for future biological tissues testing [35]. Moreover, gels are chemically and electrically stable, exhibiting a non linear elastic behaviour, as well as biological soft tissues. In particular, Pervin and Chen focused on the mechanical properties of agar gels, compared with brain matter, discovering that agar gels with concentration of 0.4~0.6% well approximate brain mechanical properties (figure 3.4) [35].

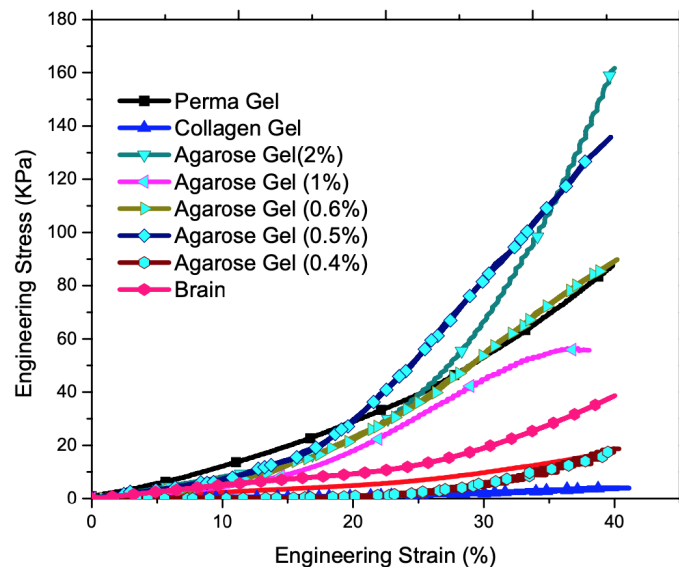


Figure 3.4 – Comparison of stress-strain curves of different gels and brain matter at 10/s strain rate deriving from uniaxial compression tests, from a study by Pervin and Chen [35].

In this work, 2% agar gels are used because easier to manipulate and and with the final goal of developing a reliable and robust testing protocol for torsion of brain tissues. Cylindrical agar gel samples are created by dissolving powdered

agarose in distilled water, heated using a hot plate and stirred until fully dissolved. The hot gel is then poured into 3D printed moulds (figure 3.5(a)) and allowed to cool at room temperature to create cylinders of various geometries. In particular, four geometries are tested in order to investigate the possible presence of any geometrical effect: 25, 20, 15 and 10 mm diameters. By using a 3D printed cutting guide (figure 3.5(b)) and a scalpel, 10 mm height samples are obtained (figure 3.6).

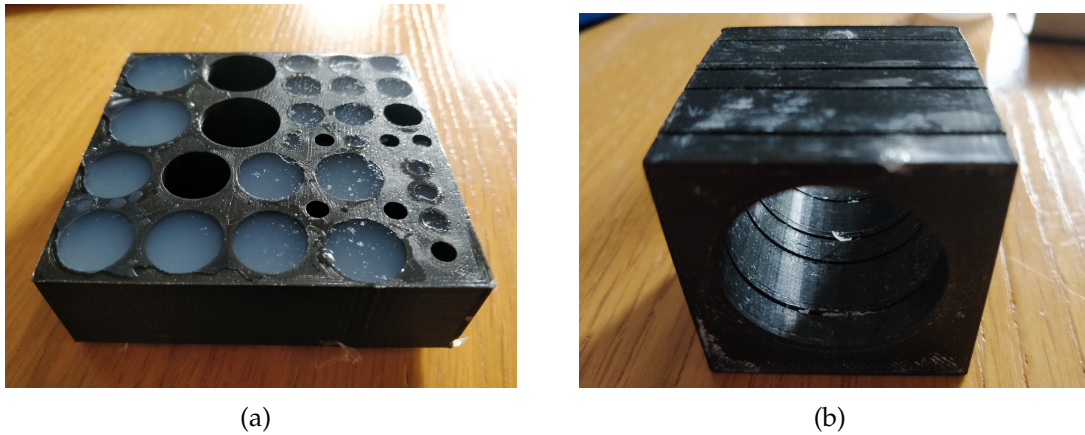


Figure 3.5 – (a) Example of a 3D printed mould with 20, 15 and 10 mm diameters holes in which the hot gel is poured; (b) 3D printed cutting guide: the sample is placed inside and is cut with a scalpel.

Experiments are conducted at room temperature (circa 23°C); in order to maintain the hydration, the 10 mm height samples are extracted from the mould just before the testing.



Figure 3.6 – Cylindrical 2% agar gels of 25, 20 and 15 mm diameters ready for testing.

3.2.2 Equipment and protocol

A modular compact rheometer *Anton Paar MCR 302* with parallel plates is used, photographed in figure 3.7. The mobile upper plate has a diameter of 25 mm, matching the diameter of the biggest sample geometry tested. The device has a *torque* resolution of 10^{-9} N · m, a *normal force* resolution of 0.01 N and a *deflection angle* resolution of 0.05×10^{-6} rad [36]. The functioning of the machine is very simple for torsion tests: after the positioning of the cylindrical sample, the upper plate starts rotating and records the desired parameters.



Figure 3.7 – Anton Paar rheometer.

The chosen velocity rotation is 1 rpm (revolutions per minute), that means a twist rate (angular velocity of the upper plate per unit height of the sample) of $10.5 \text{ rad}/(\text{m} \cdot \text{s})$. This low velocity allows to neglect the viscoelastic effects, performing a quasi-static deformation.

Now, the testing protocol will be illustrated. Once the rheometer is initialized and the 25 mm diameter plate is mounted, the "set zero gap" process starts (figure 3.8(a)): it is automatic and allows the device to measure the distance between the plates during the test. To set the zero gap, the upper plate starts going downward until it touches the bottom plate (the machine "reads" a value of the normal force different from zero) and then goes back upward, ready to measure.

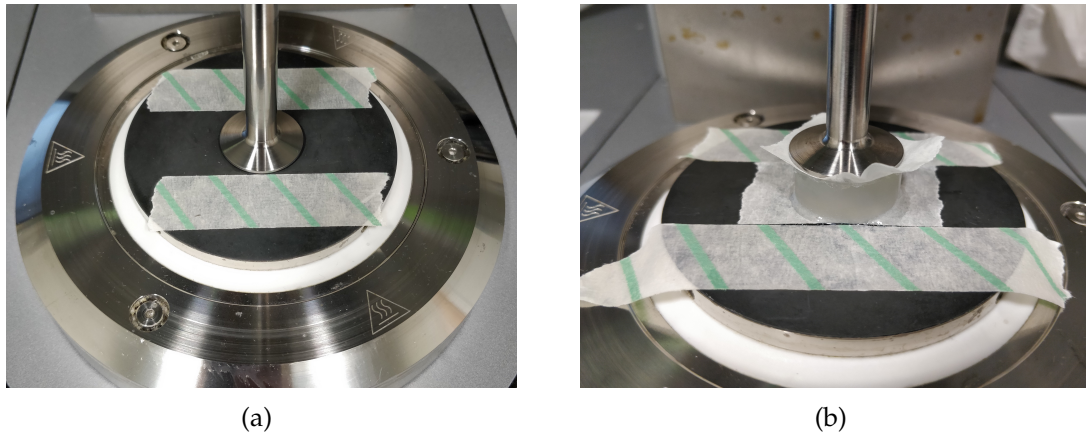


Figure 3.8 – (a) "Set zero gap" procedure: the upper plate touches the bottom plate; (b) the sample is glued and ready for twisting.

At this point, the cylindrical samples are placed: a *high viscosity glue* that works on wet materials is used, similar to the *surgical glue*, used instead of stitches during surgical operation. To enable easy removal of the tested samples and to protect the plates from glue, masking tape is applied to both plates (figure 3.8(b)), prior to the application of the glue. When the tape is positioned, the glue is applied to the bottom plate, the sample is laid in the very centre of the plate, then other glue is put on the top surface of the sample and finally the upper plate runs down. The quantity of glue is crucial because too little would cause the sample to slip, so no couple could be applied; too much would harden the entire sample and ruin the test.

The upper plate is driven down manually, until the normal force measured by the rheometer was slightly higher than 0 N: this means that the sample got minimally compressed in order to allow the glue to set. After one minute, the glue is set and the sample is stick to the plates. Before starting the twisting of the sample, it is essential to set again the normal force to zero by lifting the upper plate manually, avoiding the pre-compression of the gels during the testing.

The set-up is complete (figure 3.8(b)) and the upper plate begins rotating for a certain period of time (usually 15-20 seconds), long enough to let the sample break (figure 3.9). During the rotation, torque, normal force, deflection angle on

the top surface and gap between the plates are recorded. The gap is useful for a correct mechanical characterisation of the gels, because the height of the samples is not exactly 10 mm, due to the manual cut of the gels (the precise dimensions are reported in tables 4.1, 4.2, 4.3 and 4.4 in the next chapter). Each sample was tested once and then discarded.

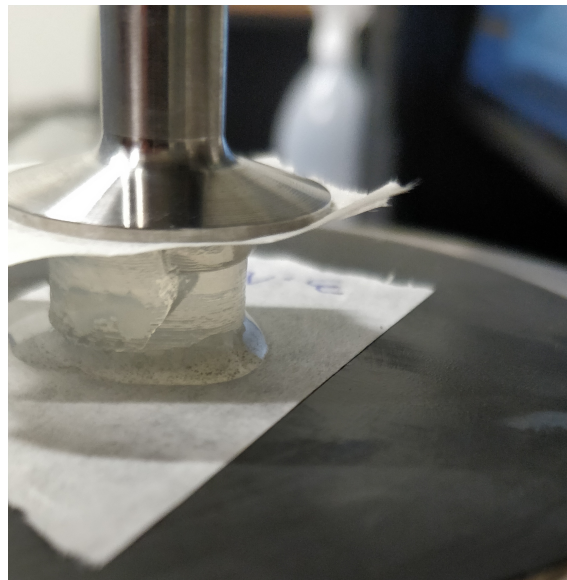


Figure 3.9 – Example of a broken sample after the test.

A remark about the normal force measured by the rheometer: as said before, the force is the consequence of the so called Poynting effect. The gels exhibit a *positive* Poynting effect, but the normal force is negative: this is because the cylindrical sample tries to expand axially, but the plates prevent the expansion, resulting in a compression of the sample and so in a negative force acting on the sample.

3.2.3 Testing issues

Throughout the testing sessions, many issues with the samples raised. There were lots of test with non-physical results. The main source of error was the glue: often the glue did not set properly and the sample slipped without producing any torque. In lots of experiments, the normal force had a strange trend, even with positive values. The positioning of the samples in the centre of the plate was essential (figure 3.10), as well as the cut from the mould, because the surfaces of the gels had to be parallel, otherwise the results would have been wrong. Besides, the gels tested at the end of the day were usually too stiff, because dehydrated and not available for the modelling.



Figure 3.10 – Example of a not centred sample.

Moreover, the presence of a compressor represented a relevant source of noise during the testing. The compressor was necessary for the functioning of the machine and was periodically active: a large number of samples were discarded because compromised by the compressor noise.

To sum up, only about 10% of the total tested samples were actually good, causing a big loss of time and materials.

Chapter 4

Experimental results

4.1 Summary of the results

In this section, a recap of the actual heights of the samples, deflection angle at the breaking point and the corresponding *twist* at the breaking point is proposed for each of the tested geometries (tables 4.1, 4.2, 4.3 and 4.4). The twist ϕ is an important parameter, very useful for the rest of the analysis and is given by

$$\phi = \frac{\alpha}{H}, \quad (4.1)$$

where α is the deflection angle and H is the initial height of the sample.

Sample	H [mm]	α_{break} [mrad]	ϕ_{break} [rad/m]
S ₁	10.04	211.30	21.04
S ₂	10.79	205.14	19.02
S ₃	10.14	158.94	15.68
S ₄	10.89	184.91	16.99
S ₅	10.47	235.83	22.53
S ₆	10.72	219.78	20.51
S ₇	9.69	206.06	21.27
S ₈	10.09	204.17	20.23
S ₉	10.30	216.43	21.01
mean±STD	10.35±0.40	204.73±21.98	19.81±2.20

Table 4.1 – Actual height, deflection angle and twist at the breaking point, with relative mean and standard deviation, for each sample of the **25 mm** diameter geometry.

Sample	H [mm]	α_{break} [mrad]	ϕ_{break} [rad/m]
S ₁	11.94	305.54	25.60
S ₂	9.62	307.44	31.95
S ₃	10.92	308.65	28.27
S ₄	10.40	313.92	30.17
S ₅	10.55	308.67	29.25
S ₆	10.23	260.61	25.48
S ₇	10.30	254.54	24.72
mean±STD	10.57±0.72	294.20±25.21	27.92±2.73

Table 4.2 – Actual height, deflection angle and twist at the breaking point, with relative mean and standard deviation, for each sample of the **20 mm** diameter geometry.

Sample	H [mm]	α_{break} [mrad]	ϕ_{break} [rad/m]
S ₁	10.02	378.72	37.82
S ₂	10.54	404.9	38.41
S ₃	9.27	349.00	37.64
S ₄	10.03	469.92	46.87
S ₅	9.94	342.96	34.50
S ₆	10.16	299.83	29.53
mean±STD	9.99±0.41	374.22±48.77	37.46±5.68

Table 4.3 – Actual height, deflection angle and twist at the breaking point, with relative mean and standard deviation, for each sample of the **15 mm** diameter geometry.

Sample	H [mm]	α_{break} [mrad]	ϕ_{break} [rad/m]
S ₁	9.55	526.46	55.05
S ₂	12.73	641.70	50.41
S ₃	8.44	452.45	53.64
S ₄	9.04	415.63	46.00
S ₅	9.86	410.85	41.67
S ₆	10.05	452.46	45.03
S ₇	9.74	433.60	44.50
S ₈	9.63	443.02	46.02
mean±STD	9.88±1.26	471.90±77.14	47.79±4.72

Table 4.4 – Actual height, deflection angle and twist at the breaking point, with relative mean and standard deviation, for each sample of the **10 mm** diameter geometry.

4.2 Choice of the model and filtering procedure

The procedure necessary to filter the obtained data of *torque* and *normal force* is explained. After this approach, the dataset is ready for model fitting and parameters estimation.

First of all, it is necessary to choose a model for the *strain energy function* in order to find a relationship between stress and strain of the gels and extract the mechanical parameters from the collected data. A *Mooney-Rivlin model* is chosen (equation for the Cauchy stress 2.40 on page 21). The theoretical Mooney-Rivlin modelling of the torsion will be explained in the next chapter, in which the analytical formulation of torque and normal force will be provided.

As shown in detail in chapter 5, the Mooney-Rivlin theory establishes that torque τ and normal force N_z vary linearly with twist ϕ and twist squared ϕ^2 , respectively. The following lines describe how to get clean data from the rheometer output. Typical rheometer output of torque and normal force are visible in figure 4.1, plotted against twist and twist squared, respectively.

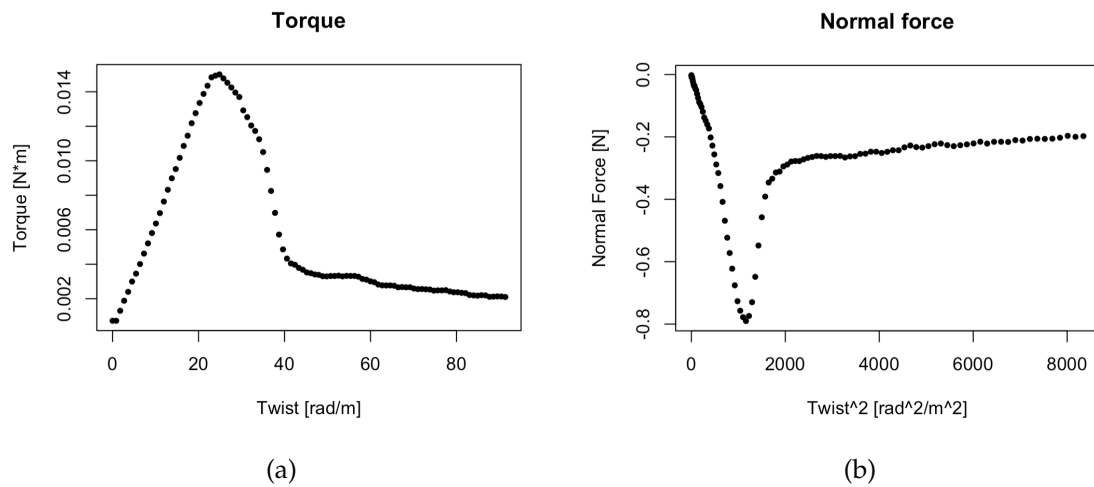


Figure 4.1 – Typical output of the rheometer for (a) torque and (b) normal force, in which it is possible to identify an initial linear region.

Both plots present a linear region up to a maximum in the case of the torque τ in figure 4.1(a) or a minimum in the case of the normal force N_z in figure 4.1(b). The maximum, or minimum, of the curves represent the breaking point of the samples (figure 3.9 on page 30) and correspond with a sudden change in the mechanical properties. Hence, the data of torque and normal force after this values are discarded.

4.3 Filtered data

The filtering of raw data is obtained with the open-source software RStudio.

Filtered data of torque τ and normal force N_z plotted against twist ϕ and twist squared ϕ^2 , respectively, are provided in the following images. They are grouped by sample diameter, 25 mm in figure 4.2, 20 mm in figure 4.3, 15 mm in figure 4.4 and 10 mm in figure 4.5.

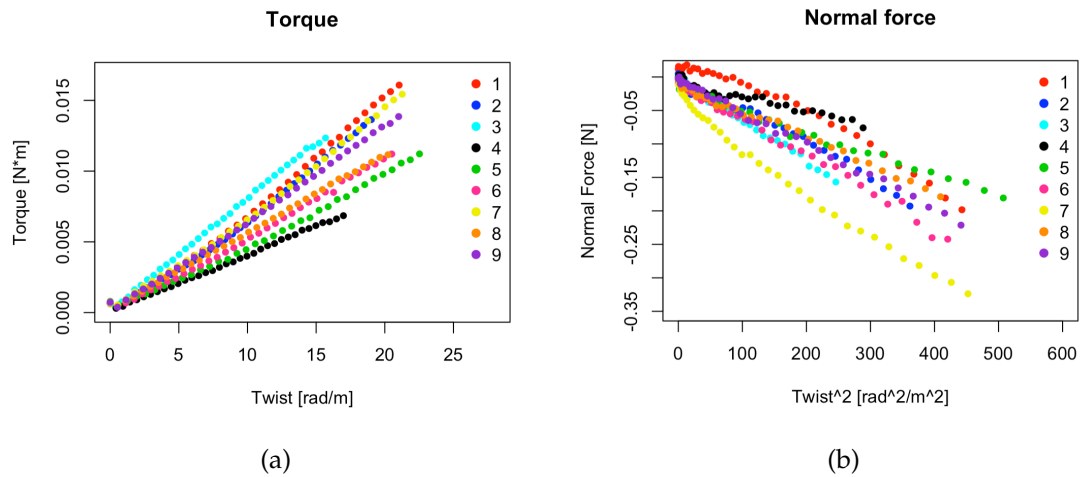


Figure 4.2 – (a) Filtered torque τ vs twist ϕ and (b) normal force N_z vs twist squared ϕ^2 for 25 mm diameter samples.

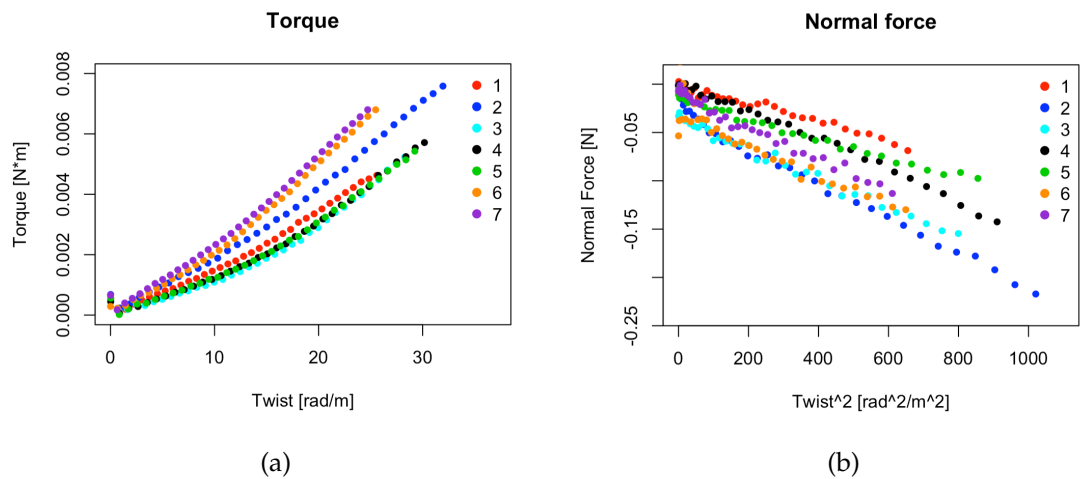


Figure 4.3 – (a) Filtered torque τ vs twist ϕ and (b) normal force N_z vs twist squared ϕ^2 for 20 mm diameter samples.

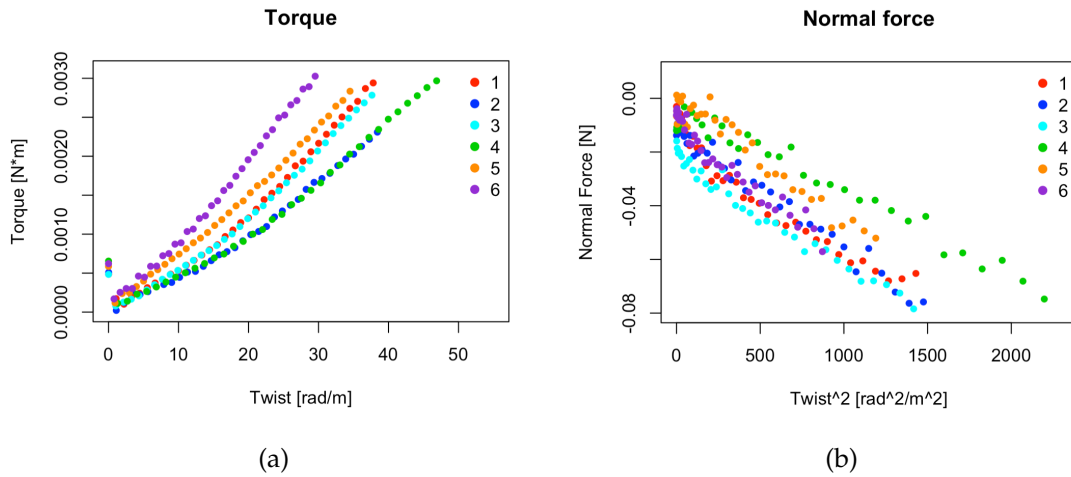


Figure 4.4 – (a) Filtered torque τ vs twist ϕ and (b) normal force N_z vs twist squared ϕ^2 for 15 mm diameter samples.

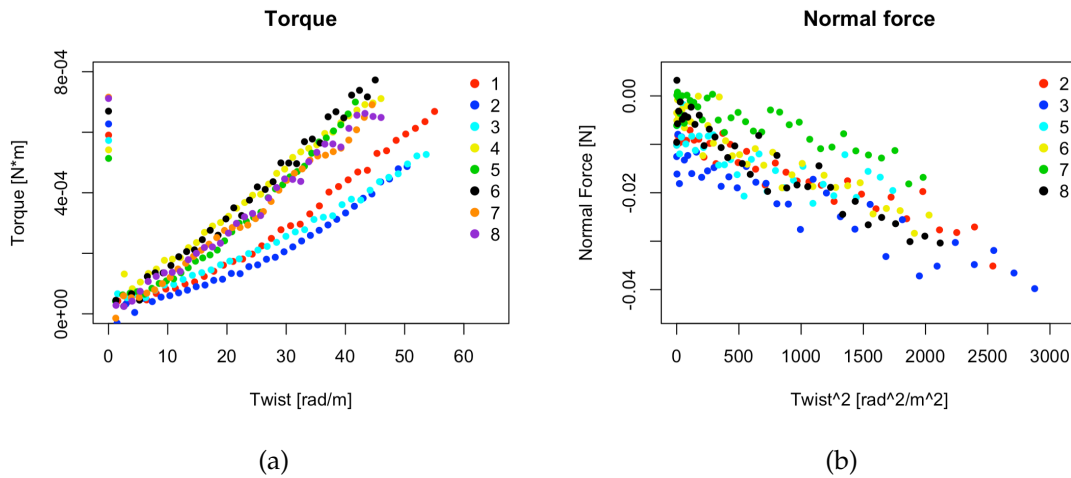


Figure 4.5 – (a) Filtered torque τ vs twist ϕ and (b) normal force N_z vs twist squared ϕ^2 for 10 mm diameter samples.

Normal force from sample 1 and 4 of the 10 mm geometry (figure 4.5(b)) are not plotted because affected by the huge noise deriving from the compressor (as explained in section 3.2.3 on page 30). Nevertheless, the data are not discarded, resulting useful for the following analysis.

In figure 4.6, the mean torque 4.6(a) and normal force 4.6(b) with relative standard deviation are represented, with all the geometries plotted together.

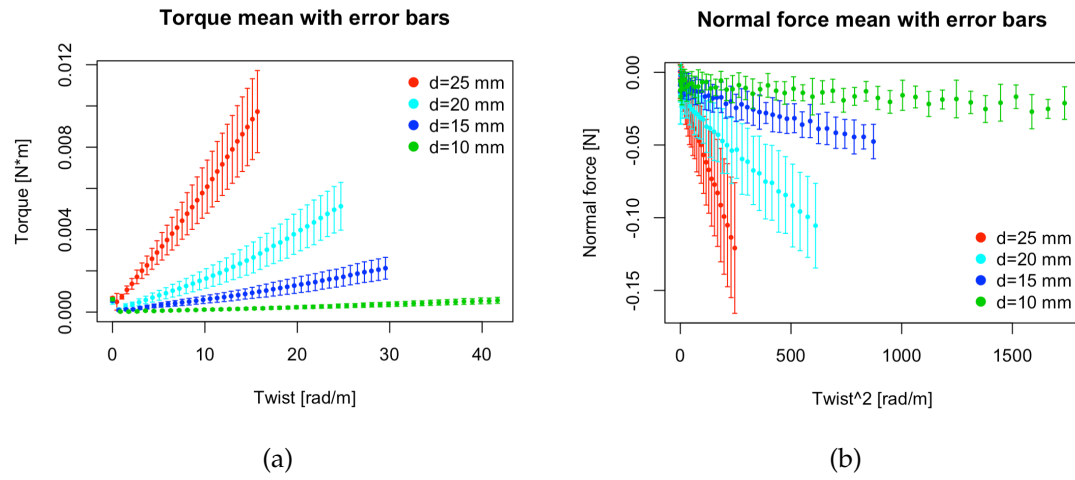


Figure 4.6 – (a) Mean torque and standard deviation and (b) mean normal force and standard deviation for all geometries.

4.3.1 Comments

An initial noisy region is noticeable in the torque plots, especially when the diameter decreases (i.e. 15 mm, figure 4.4(a) and 10 mm, figure 4.5(a)): this is due to the initial plate velocity, smaller than the fully operational velocity of $n=1$ rpm at the very beginning of the test. Therefore, the first points are discarded.

Moreover, with the decrease of the ratio between sample diameter and sample height, a greater deformability of the gels has been observed, resulting in higher values of both the deflection angle and the twist reached before the fracture. As a matter of fact, 10 mm diameter samples break at a deflection angle of about 472 mrad on average (corresponding to a twist of 48 rad/m), compared to 205 mrad (corresponding to a twist of 20 rad/m) for the 25 mm diameter geometry (data from tables 4.4 and 4.1). Nevertheless, the mean *strain* at which the fracture occurs is similar for every geometry. The strain γ for a cylinder undergoing a rotational deformation is defined as:

$$\gamma = \frac{\alpha}{H}r, \quad (4.2)$$

where α is the deflection angle, H is the height of the sample and r is its radius. Table 4.5 shows the mean strains at the break point for each tested geometry.

	d = 25 mm	d = 20 mm	d = 15 mm	10 d = mm
γ_{break} [rad]	0.25	0.28	0.28	0.24

Table 4.5 – Mean strains in radians at the break point for each sample geometry.

As expected, the strain is in the same range for every geometry, as the gels are made of the same material.

Last remark: the normal force gets more scattered with smaller diameter samples, especially for 10 mm diameter. This is due to lower values of the recorded force (close to the device sensibility), becoming more affected by surrounding noise in the laboratory. Besides, the glue might affect more the results, because of the reduced available surface.

Chapter 5

Modelling

In this chapter, a quantitative estimation of the mechanical behaviour of the gels in torsion will be provided. Firstly, the simple torsion will be modelled theoretically, then the experimental data will be fitted and finally the tests will be reproduced with Finite Element simulations in Abaqus.

5.1 Theory

In this section, analytical formulations of *torque* and *normal force* are obtained for a cylinder made of an incompressible, isotropic, homogeneous, hyperelastic material, undergoing simple torsion at very low velocity. The cylinder has initial radius R_0 and height H_0 and final radius r_0 and height h_0 . The kinematics of the deformation is defined by $\mathbf{x}(r, \theta, z) = \chi \mathbf{X}(R, \Theta, Z)$, where (r, θ, z) and (R, Θ, Z) are the current and reference configuration in cylindrical coordinates (figure 5.1) [37].

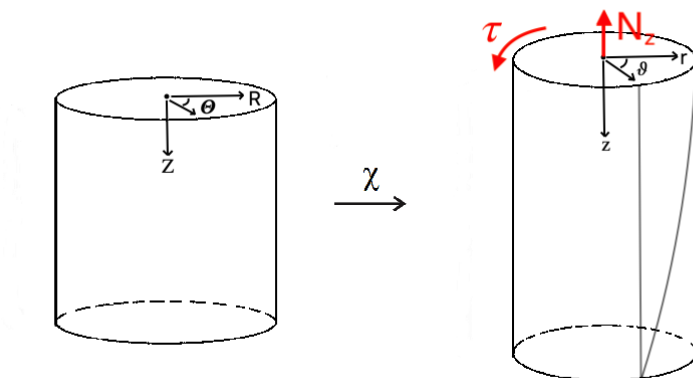


Figure 5.1 – Schematic representation of the simple torsion of a cylinder with initial radius R_0 and height H_0 and final radius r_0 and height h_0 , in cylindrical coordinates; torque and normal force are also displayed.

As illustrated in chapter 3, before proceeding with the testing, the upper plate is moved upwards in order to obtain a null normal force and, therefore, a non precompressed cylinder. Nevertheless, variations of the force within the range of the rheometer sensitivity (0.01 N) are not sensed by the device. So it is reasonable to expect a tiny contraction of the sample at the beginning of the test [4]. The consequence is the addition of an axial contraction to the torsion of the cylinder, resulting in the following deformation, written in cylindrical coordinates:

$$\begin{cases} r = R/\sqrt{\lambda}, \\ \theta = \Theta + \phi\lambda Z, \\ z = \lambda Z, \end{cases} \quad (5.1)$$

where λ is the uniform stretching ratio in the axial direction, $\phi = \alpha/(\lambda H_0)$ is the twist per unit height and α is the angle of rotation in radians. In particular, the equation for the radius in the deformed configuration (first equation of (5.1)) is obtained by imposing the incompressibility of the cylinder.

The deformation gradient F has the following components ($F_{ij} = \partial x_i / \partial X_j$) then:

$$F = \begin{pmatrix} 1/\sqrt{\lambda} & 0 & 0 \\ 0 & 1/\sqrt{\lambda} & r\phi\lambda \\ 0 & 0 & \lambda \end{pmatrix}, \quad (5.2)$$

so $\det F = 1$, necessary condition for the cylinder to be incompressible (from equation 2.35).

The left Cauchy-Green deformation tensor $B = FF^T$ and its inverse B^{-1} are:

$$B = \begin{pmatrix} 1/\lambda & 0 & 0 \\ 0 & 1/\lambda + \phi^2\lambda^2r^2 & \phi\lambda^2r \\ 0 & \phi\lambda^2r & \lambda^2 \end{pmatrix}, \quad B^{-1} = \begin{pmatrix} \lambda & 0 & 0 \\ 0 & \lambda & -r\phi\lambda \\ 0 & -r\phi\lambda & \phi^2\lambda r^2 + 1/\lambda^2 \end{pmatrix}. \quad (5.3)$$

The principal invariants of B are found to be:

$$I_1 = \text{tr}[B] = \frac{2}{\lambda} + \lambda^2(1 + \phi^2\lambda^2), \quad I_2 = \text{tr}[B^{-1}] = \lambda(2 + \phi^2r^2) + \frac{1}{\lambda^2}. \quad (5.4)$$

The principal stretches are the square roots of the eigenvalues of B . The stretch $\lambda_1 = 1$ is the intermediate stretch and corresponds with the radial direction, while the maximum and minimum stretches λ_2 and λ_3 are obtained by solving the following equations:

$$(\lambda_2\lambda_3)^2 = \frac{1}{\lambda}, \quad \lambda_2^2 + \lambda_3^2 = \frac{1}{\lambda} + \lambda^2 + (\lambda\phi r)^2. \quad (5.5)$$

5.1.1 Choice of the strain energy function

As anticipated in the previous chapter, a Mooney-Rivlin strain energy function is chosen to model the data: this choice is motivated by the linearity of torque and normal force with respect to twist and twist squared, highlighted in figure 4.2, 4.3, 4.4 and 4.5. Recalling equation (2.40), the strain energy function is:

$$W = C_1(I_1 - 3) + C_2(I_2 - 3), \quad (5.6)$$

where C_1 and C_2 are constants and I_1, I_2 are the principal invariants of \mathbf{B} . For this model, a fundamental parameter, called *shear modulus*, is defined as $\mu = 2(C_1 + C_2)$. The corresponding constitutive equation for the Cauchy stress σ is:

$$\sigma = -p\mathbf{I} + 2C_1\mathbf{B} - 2C_2\mathbf{B}^{-1}, \quad (5.7)$$

where p is a Lagrange multiplier emerging from the incompressibility constraint 2.35.

Now, the Cauchy stress σ can be decomposed in its components by substituting the left Cauchy-Green deformation tensor \mathbf{B} and its inverse \mathbf{B}^{-1} (5.4), in equation (5.7):

$$\begin{aligned} \sigma_{rr} &= 2C_1\lambda^{-1} - 2C_2\lambda - p, \\ \sigma_{\theta\theta} &= 2C_1(\lambda^{-1} + \phi^2\lambda^2r^2) - 2C_2\lambda - p, \\ \sigma_{zz} &= 2C_1\lambda^2 - 2C_2(\phi^2\lambda r^2 + \lambda^{-2}) - p, \\ \sigma_{\theta z} &= \sigma_{z\theta} = 2C_1\phi r\lambda^2 - 2C_2\phi r\lambda, \\ \sigma_{r\theta} &= \sigma_{rz} = \sigma_{\theta r} = \sigma_{zr} = 0. \end{aligned} \quad (5.8)$$

In order to find a solution for the Lagrange multiplier p , the *equation of motion* (2.25) is used, in the absence of body forces and with a negligible acceleration due to the quasi-static deformation ($\mathbf{a} = \mathbf{b} = 0$), so it becomes:

$$\operatorname{div}\sigma = 0. \quad (5.9)$$

Since the lateral surface of the cylinder is stress-free, the next boundary condition is added:

$$\sigma_{rr}(r_0) = 0. \quad (5.10)$$

Considering only the non zero terms, equation (5.9) can be written as follows

in cylindrical coordinates, along with the boundary condition (5.10):

$$\begin{cases} \frac{\partial \sigma_{rr}}{\partial r} + \frac{\sigma_{rr} - \sigma_{\theta\theta}}{r} = 0, \\ \frac{1}{r} \frac{\partial \sigma_{\theta\theta}}{\partial \theta} = 0, \\ \frac{\partial \sigma_{zz}}{\partial z} = 0, \\ \sigma_{rr}(r_0) = 0. \end{cases} \quad (5.11)$$

From (5.8) and (5.11), it is clear that the Lagrange multiplier p only depends on radial variable r and not on θ and z , so the system (5.11) becomes:

$$\begin{cases} \frac{\partial \sigma_{rr}(r)}{\partial r} + \frac{\sigma_{rr}(r) - \sigma_{\theta\theta}(r)}{r} = 0, \\ \sigma_{rr}(r_0) = 0. \end{cases} \quad (5.12)$$

To solve (5.12), the first equation of the system is integrated accounting for the boundary condition (5.10), obtaining:

$$\sigma_{rr}(r) = \int_r^{r_0} \frac{\sigma_{rr}(r) - \sigma_{\theta\theta}(r)}{r} dr. \quad (5.13)$$

Now, substituting (5.8) in (5.13), an expression for the Lagrange multiplier p is obtained:

$$\begin{aligned} p(r) &= \frac{2C_1}{\lambda} - 2C_2\lambda + \int_r^{r_0} 2C_1\phi^2\lambda^2 r dr \\ &= C_1 \left[\frac{2}{\lambda} + \phi^2\lambda^2(r_0^2 - r^2) \right] - 2C_2\lambda, \end{aligned} \quad (5.14)$$

and filling (5.14) in (5.8), the components of the Cauchy stress σ can be calculated, depending on the radius r only:

$$\begin{aligned} \sigma_{rr}(r) &= C_1(r^2 - r_0^2)\lambda^2\phi^2, \\ \sigma_{\theta\theta}(r) &= C_1(3r^2 - r_0^2)\lambda^2\phi^2, \\ \sigma_{zz}(r) &= C_1 \left[2\frac{\lambda^3 - 1}{\lambda} + (r^2 - r_0^2)\lambda^2\phi^2 \right] + 2C_2 \left(\frac{\lambda^3 - 1}{\lambda^2} + r^2\lambda\phi^2 \right), \\ \sigma_{\theta z}(r) &= 2(C_2 + C_1\lambda)r\lambda\phi. \end{aligned} \quad (5.15)$$

5.1.2 Analytic expression of torque and normal force

Finally, it is possible to compute the torque τ and the normal force N_z required to maintain the finite torsion and stretching deformation described in (5.1), reminding that $r_0=R_0/\sqrt{\lambda}$:

$$\begin{aligned}\tau &= 2\pi \int_0^{R_0/\sqrt{\lambda}} r^2 \sigma_{\theta z}(r) dr \\ &= \pi R_0^4 \left(C_1 + \frac{C_2}{\lambda} \right) \phi \\ &= \mathcal{A}\phi,\end{aligned}\tag{5.16}$$

$$\begin{aligned}N_z &= 2\pi \int_0^{R_0/\sqrt{\lambda}} r \sigma_{zz}(r) dr \\ &= -2\pi R_0^2 \left(C_1 + \frac{C_2}{\lambda} \right) \left(\frac{1-\lambda^3}{\lambda^2} \right) - \pi R_0^4 \left(\frac{C_1}{2} + \frac{C_2}{\lambda} \right) \phi^2 \\ &= \mathcal{C} + \mathcal{B}\phi^2.\end{aligned}\tag{5.17}$$

The constants \mathcal{A} , \mathcal{B} and \mathcal{C} are related to the Mooney-Rivlin parameters C_1 and C_2 by

$$C_1 = 2\frac{\mathcal{A} + \mathcal{B}}{\pi R_0^4}, \quad \frac{C_2}{\lambda} = -\frac{\mathcal{A} + 2\mathcal{B}}{\pi R_0^4},\tag{5.18}$$

and the stretching ratio λ is the unique real and positive root of the following cubic equation [4]:

$$2\mathcal{A}(\lambda^3 - 1) - \mathcal{C}R_0^2\lambda^2 = 0.\tag{5.19}$$

Equations 5.16 and 5.17 clearly show the linear dependence of the torque on the twist and of the normal force on the twist squared. The coefficient \mathcal{B} is associated with the Poynting effect exhibited by the sample and is due almost entirely to the twist, whereas the coefficient \mathcal{C} is related to the precompression of the sample. In *pure torsion*, when the sample is not compressed at all (i.e $\lambda = 1$), $\mathcal{C} = 0$ and \mathcal{B} provides an effective measure of the exact Poynting effect [4].

5.2 Parameters estimation

In this section, the Mooney-Rivlin parameters C_1 , C_2 and the *shear modulus* μ are obtained for each set of data.

The constants \mathcal{A} , \mathcal{B} and \mathcal{C} , introduced in section 5.1, are calculated by fitting the experimental data in figures 4.2, 4.3, 4.4 and 4.5. The RStudio function “lm” has been used to perform a linear regression on the data sets $\{\phi, \tau\}$ and $\{\phi^2, N_z\}$.

In particular, from the $\{\phi, \tau\}$ data set, the linear regression returns \mathcal{A} , i.e. the angular coefficient of the fitted straight line (from equation 5.16), in red in figure 5.2(a). From $\{\phi^2, N_z\}$, the linear regression returns \mathcal{B} and \mathcal{C} , i.e. angular coefficient and intercept of the fitted straight line (from equation 5.17), in red in figure 5.2(b).

In figure 5.2, an example of data fitting is proposed for a 25 mm diameter sample.

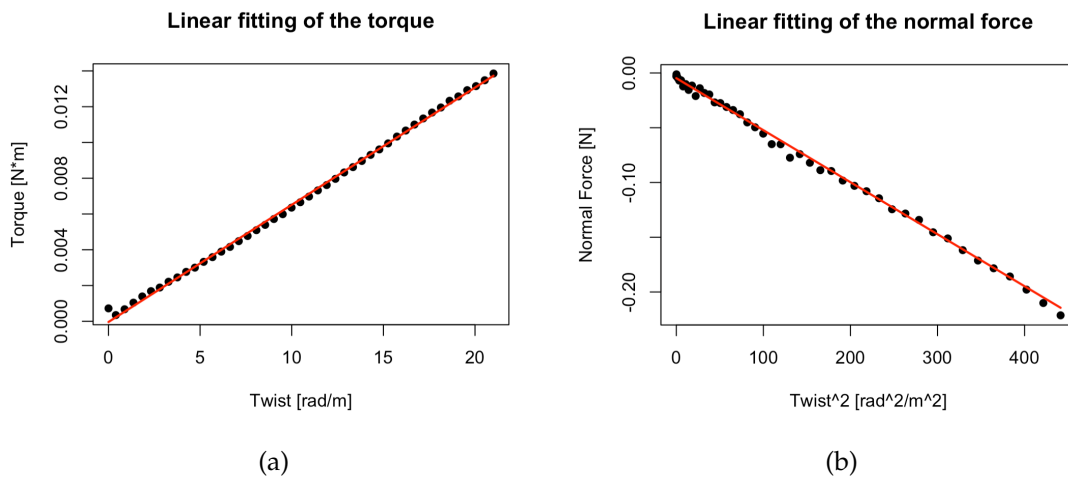


Figure 5.2 – Example of fitting for (a) torque and (b) normal force of a 25 mm diameter sample.

In the case displayed in figure 5.2, the *coefficients of determination* calculated with the linear regression are $R_\tau^2 = 0.999$, for the torque, and $R_N^2 = 0.997$, for the normal force.

Once the constants \mathcal{A} , \mathcal{B} and \mathcal{C} are extracted, the Mooney-Rivlin parameters C_1 , C_2 and the stretching ratio λ are determined solving in MATLAB the equations (5.18) and (5.19). Consequently, the shear modulus $\mu = 2(C_1 + C_2)$ is easily calculated.

The elastic properties of the gels are presented in tables 5.1, 5.2, 5.3 and 5.4. The Mooney-Rivlin constant C_2 and the shear modulus μ are the most characterizing parameters for a soft tissue. Their values for every sample geometry are included in the tables, along with their mean and standard deviation. Besides, the stretching ratio λ and the coefficients of determination for torque and normal force, derived from the linear regression, are shown.

Sample	C_2 [Pa]	μ [Pa]	λ	R_τ^2	R_N^2
S ₁	1618	20050	0.99	0.995	0.970
S ₂	3329	18680	1.00	0.994	0.987
S ₃	5717	20638	1.00	0.999	0.995
S ₄	738	10451	0.99	0.999	0.944
S ₅	2139	12747	1.00	0.995	0.985
S ₆	6744	14280	0.99	0.997	0.989
S ₇	8731	18625	0.98	0.996	0.986
S ₈	3424	14294	0.99	0.999	0.994
S ₉	3839	17091	0.99	0.999	0.997
mean±STD	4031±2584	16317±3527			

Table 5.1 – Estimated elastic parameters for 25 mm diameter samples: Mooney-Rivlin parameter C_2 , the shear modulus μ , the stretching ratio λ and the coefficients of determination for torque R_τ^2 and normal force R_N^2 ; in the last row, mean and standard deviation for C_2 and μ are evaluated.

Sample	C_2 [Pa]	μ [Pa]	λ	R_τ^2	R_N^2
S ₁	277	11096	0.99	0.988	0.969
S ₂	5122	14037	0.98	0.986	0.983
S ₃	4722	10298	0.96	0.961	0.985
S ₄	4135	10906	0.99	0.975	0.990
S ₅	1354	10704	0.98	0.976	0.976
S ₆	3516	16594	0.97	0.988	0.860
S ₇	2481	16918	0.97	0.991	0.979
mean±STD	3087±1796	12936±2884			

Table 5.2 – Estimated elastic parameters for 20 mm diameter samples: Mooney-Rivlin parameter C_2 , the shear modulus μ , the stretching ratio λ and the coefficients of determination for torque R_τ^2 and normal force R_N^2 ; in the last row, mean and standard deviation for C_2 and μ are evaluated.

As it can be noted from table 5.4, the coefficient of determination for the normal force of 10 mm diameter samples is quite low generally. As pointed out in section 4.3.1, this is due to the scattered experimental data. The smaller values of recorded force for this geometry are more affected by the environmental noise, because close to the device sensibility. In particular, samples 1, 4 and 5 show an extremely low coefficient of determination for the normal force: the reason is the activation of a compressor during the testing, as explained in section 3.2.3.

The great difference in the computed values of the Mooney-Rivlin parameter C_2 might be attributed to the period of the day in which the tests have been

performed: as a matter of fact, the gels become stiffer while waiting to be tested, changing their mechanical properties.

Sample	C_2 [Pa]	μ [Pa]	λ	R_τ^2	R_N^2
S ₁	2501	13935	0.96	0.977	0.940
S ₂	3785	10507	0.96	0.971	0.966
S ₃	1745	13349	0.94	0.982	0.968
S ₄	402	11025	0.98	0.975	0.970
S ₅	1298	15392	0.99	0.991	0.961
S ₆	372	19939	0.97	0.991	0.906
mean±STD	1684±1311	14025±3426			

Table 5.3 – Estimated elastic parameters for **15 mm** diameter samples: Mooney-Rivlin parameter C_2 , the shear modulus μ , the stretching ratio λ and the coefficients of determination for torque R_τ^2 and normal force R_N^2 ; in the last row, mean and standard deviation for C_2 and μ are evaluated.

Sample	C_2 [Pa]	μ [Pa]	λ	R_τ^2	R_N^2
S ₁	304	11813	0.93	0.972	0.127
S ₂	3194	9036	0.95	0.964	0.790
S ₃	4101	9016	0.94	0.986	0.830
S ₄	5377	15846	0.91	0.991	0.535
S ₅	254	17213	0.95	0.984	0.640
S ₆	3664	17513	0.97	0.987	0.836
S ₇	611	15279	0.99	0.984	0.732
S ₈	5850	15571	0.97	0.983	0.890
mean±STD	2919±2265	13911±3472			

Table 5.4 – Estimated elastic parameters for **10 mm** diameter samples: Mooney-Rivlin parameter C_2 , the shear modulus μ , the stretching ratio λ and the coefficients of determination for torque R_τ^2 and normal force R_N^2 ; in the last row, mean and standard deviation for C_2 and μ are evaluated.

5.3 Computational validation

In this section, the Finite Element simulations in Abaqus are presented. First of all, the procedure is explained, then the results of simulations are compared with the experimental data and theory.

5.3.1 Procedure

The torsion simulations have been performed in Abaqus 3DEXPERIENCE R2019x Standard, using implicit analysis.

Four specimens have been chosen to be tested, one for each geometry. In particular, sample S_3 for the 25 mm diameter geometry, sample S_7 for the 20 mm diameter geometry, sample S_5 for the 15 mm diameter geometry and sample S_6 for the 10 mm diameter geometry.

First of all, the cylinder are created through the extrusion of a circle (figure 5.3). The height of the samples are reported in tables 4.1, 4.2, 4.3 and 4.4.

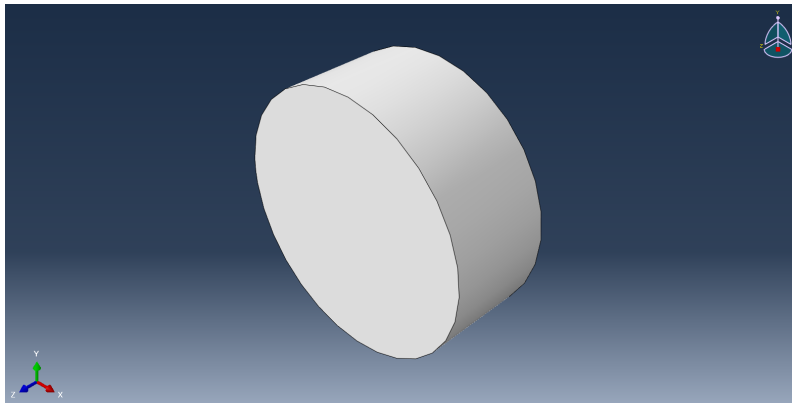


Figure 5.3 – Creation of a cylinder on Abaqus.

Then the material properties are assigned to the cylinder, choosing a hyperelastic behaviour with Mooney-Rivlin strain energy function and setting the Mooney-Rivlin constants from tables 5.1, 5.2, 5.3 and 5.4, along with the density of the gel. The "Nlgeom" configuration is activated, accounting for "non linear effects of large displacements".

At this point, the time step is set. A static general procedure is selected and the increments are summarised in table 5.5.

Initial increment	Minimum increment	Maximum increment
10^{-1}	10^{-5}	10^{-1}

Table 5.5 – Time increments for Abaqus simulations.

To simulate the behaviour of the glue on the bottom face of the cylinder, an "encastre" is applied, blocking every degree of freedom (DOF). To simulate the torsion, a reference point is created, coupled with all points of the top surface (figure 5.4). A rotation around the longitudinal axis is imposed (through a "linear ramp"), preventing every other movement. The rotational velocity of the upper

plate is set to $n = 1$ rpm, the same of the experimental testing. The chosen angle of rotation is the deflection angle at the braking point, taken from tables 4.1, 4.2, 4.3 and 4.4.

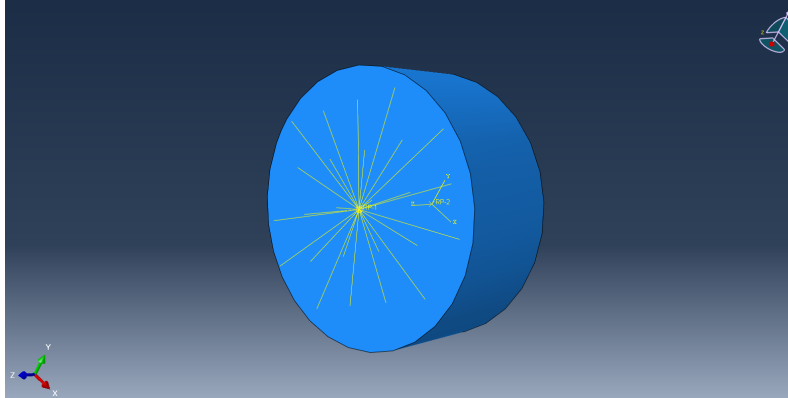


Figure 5.4 – Coupling of the top surface of the cylinder to the reference point.

Then, the mesh is created, using a 8-node linear brick C3D8RH element type with hybrid formulation to reproduce exact incompressibility (figure 5.5). The details of the mesh (i.e. number of elements and nodes created) for each geometry tested is presented in table 5.6.

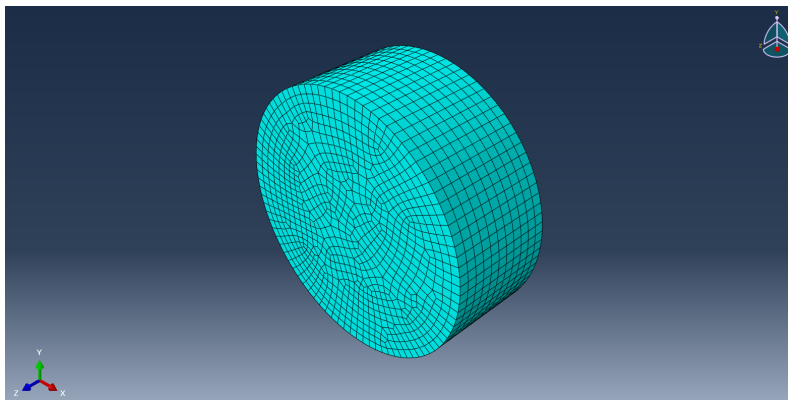


Figure 5.5 – Example of mesh on Abaqus.

Sample diameter	Number of elements	Number of nodes
25 mm	10344	22150
20 mm	13380	28390
15 mm	17138	36100
10 mm	11814	24972

Table 5.6 – Details of the mesh for each geometry tested.

Finally, the output variables RM3 and RF3 are chosen in order to display torque and normal force of the samples during the simulated rotation, respectively.

5.3.2 Results

Figures 5.6, 5.7, 5.8 and 5.9 show the comparison of torque and normal force, for each sample geometry, between experimental data, numerical simulations in Abaqus and analytical predictions from the theory of torsion presented in section 5.1 (equations (5.16) and (5.17), specifically).

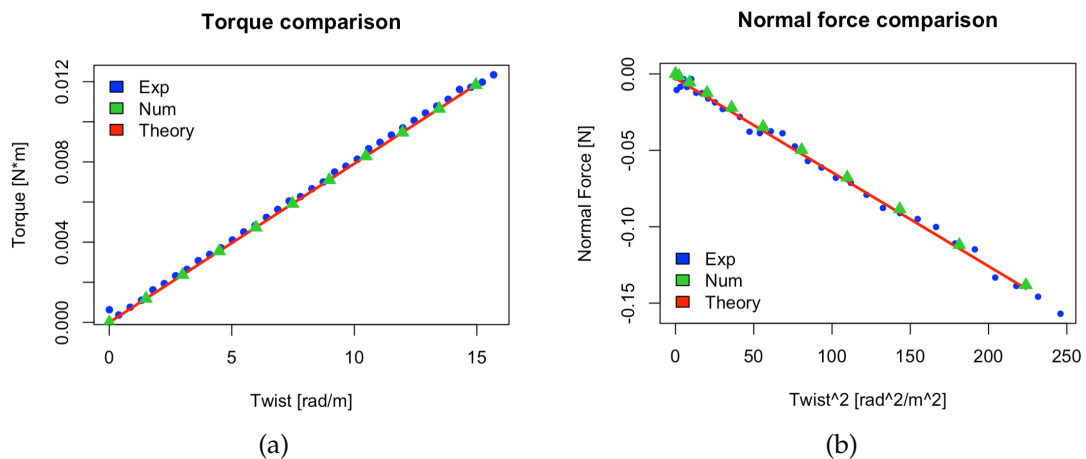


Figure 5.6 – 25 mm diameter sample S₃: comparison of (a) torque and (b) normal force between experimental data (blue circles), numerical simulations (green triangles) and "theory" (red solid line).

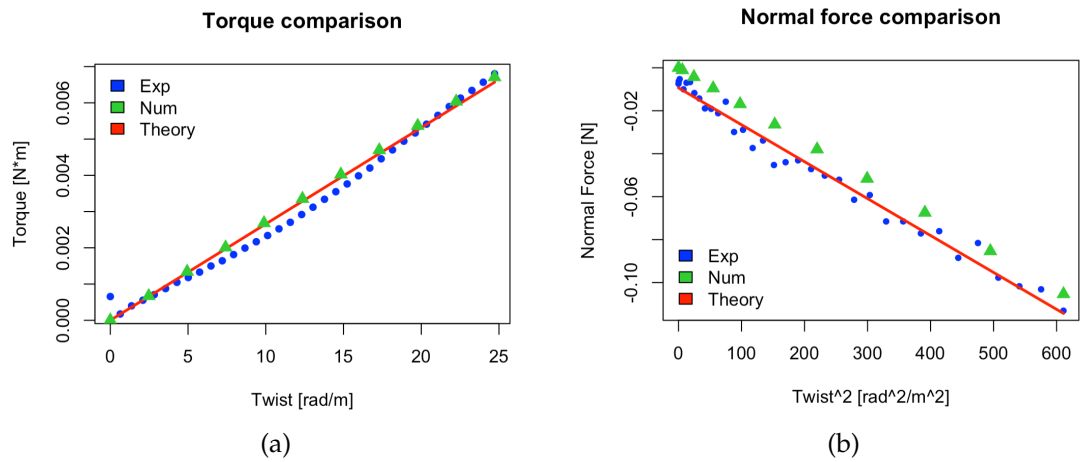


Figure 5.7 – 20 mm diameter sample S₇: comparison of (a) torque and (b) normal force between experimental data (blue circles), numerical simulations (green triangles) and "theory" (red solid line).

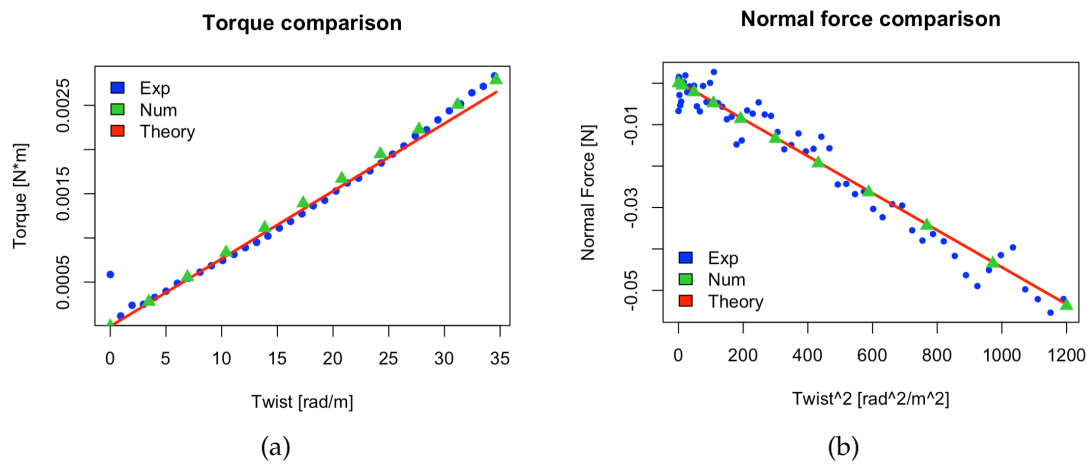


Figure 5.8 – 15 mm diameter sample S₅: comparison of (a) torque and (b) normal force between experimental data (blue circles), numerical simulations (green triangles) and "theory" (red solid line).

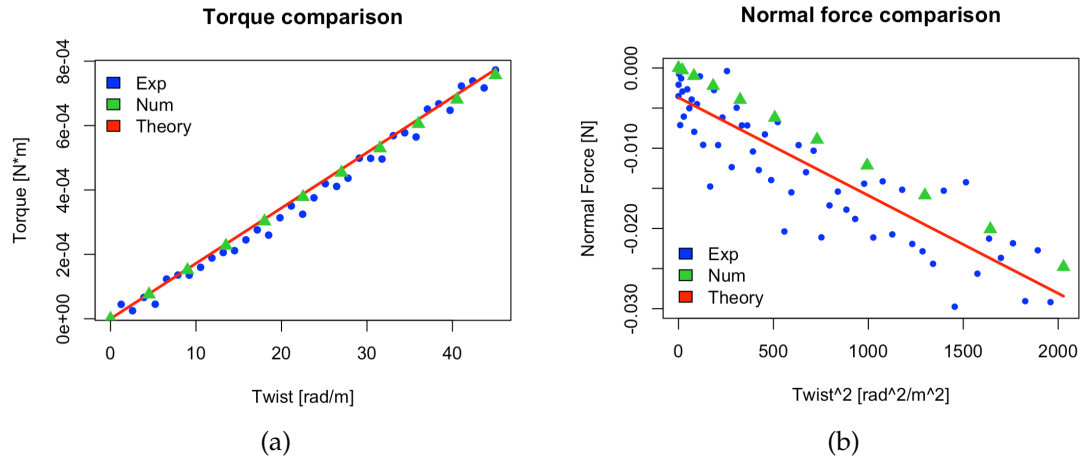


Figure 5.9 – 10 mm diameter sample S₆: comparison of (a) torque and (b) normal force between experimental data (blue circles), numerical simulations (green triangles) and "theory" (red solid line).

Numerical results are in good agreement with analytical predictions, regarding the torque (figures 5.6(a), 5.7(a), 5.8(a) and 5.9(a)). For the normal force of the 20 mm sample diameter and the 10 mm sample diameter, a small mismatch can be noted between Abaqus simulations and analytical predictions: this is mainly due to the precompression of the samples. As a matter of fact, the intercept of the red straight lines in figures 5.7(b) and 5.9(b) is not perfectly zero, but slightly less, according to the stretching ratio λ in tables 5.1, 5.2, 5.3 and 5.4.

Chapter 6

Conclusions

In the final chapter, a basic statistical analysis on the obtained data is performed.

The shear modulus μ and the Mooney-Rivlin parameter C_2 data are represented in the scatter plots of figures 6.1(a) and 6.1(b), respectively, divided in sample diameter groups.

Moreover, also the box plots for the same sets of data have been created, in figure 6.2(a) and 6.2(b). In particular, the whiskers represent the minimum and maximum values assumed by the group, the lower and upper part of the boxes correspond to the 25th and 75th percentile respectively, while the red lines are the medians of each group.

First of all, a one-way analysis of variance (ANOVA) is done on MATLAB. This analysis returns the following *p-values*: $p_\mu = 0.2364$ for the shear modulus μ and $p_{C_2} = 0.2437$ for the Mooney-Rivlin parameter C_2 . Both the *p-values* are much bigger than the alpha value of 0.05, so the null hypothesis cannot be rejected and the means of μ and C_2 of every geometry group are not statistically different.

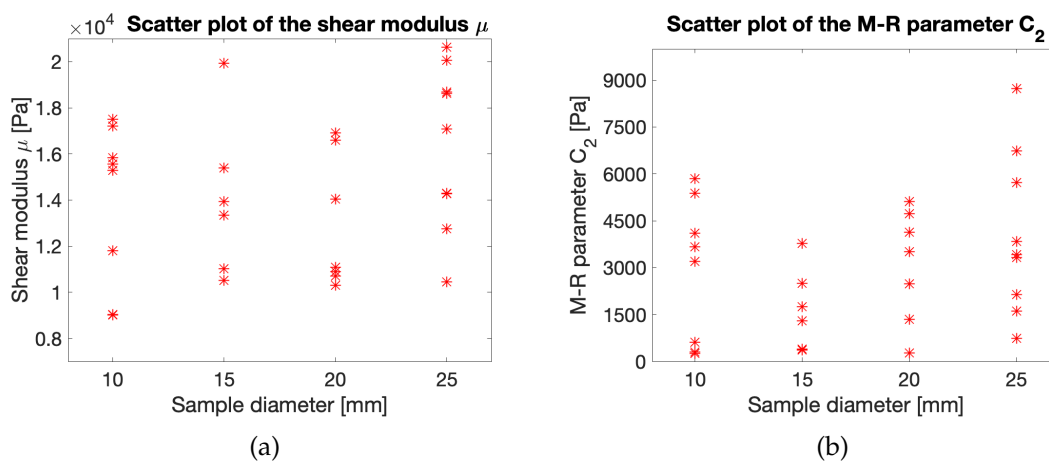


Figure 6.1 – Scatter plot of (a) μ and (b) C_2 , for every sample diameter group.

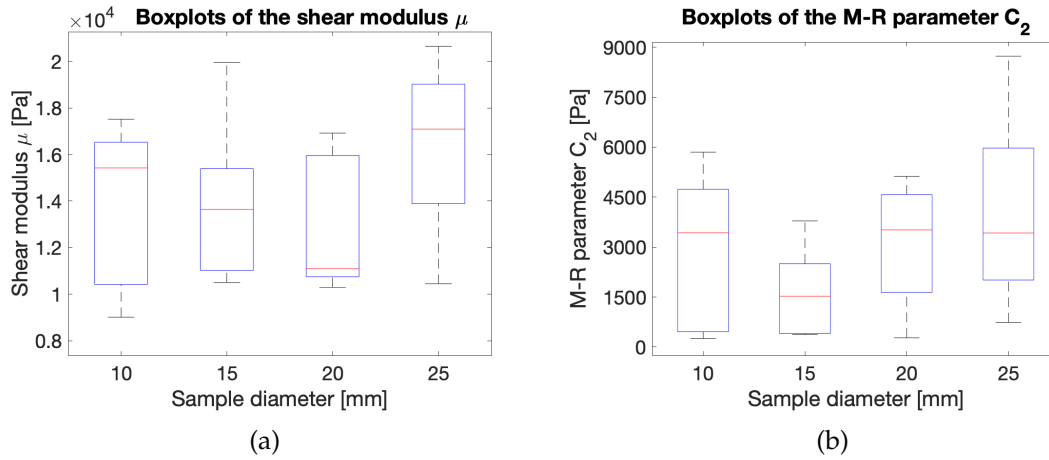


Figure 6.2 – Box plots of (a) μ and (b) C_2 , for every sample diameter group.

This might be noted from the box plots in figure 6.2, but, in order to compare the geometries two by two, a Post Hoc analysis is performed through the "multcompare" command in MATLAB.

As a matter of fact, a multiple comparison test determines which pairs of group means are significantly different. The results of this comparison, in form of p-values, are shown in tables 6.1 and 6.2 for μ and C_2 , respectively.

As expected, the p-values for each pair of geometries are much larger than 0.05, confirming that there is not any statistical difference between the estimated parameters from the four different geometries.

Group 1	Group 2	p-value
10	15	0.9999
10	20	0.9425
10	25	0.4655
15	20	0.9362
15	25	0.5730
20	25	0.2137

Table 6.1 – Obtained p-values comparing μ for every pair of sample diameter groups; 10, 15, 20 and 25 indicate 10 mm, 15 mm, 20 mm and 25 mm sample diameter groups.

Group 1	Group 2	p-value
10	15	0.7063
10	20	0.9987
10	25	0.7064
15	20	0.6401
15	25	0.1808
20	25	0.8142

Table 6.2 – Obtained p-values comparing of C_2 for every pair of sample diameter groups; 10, 15,20 and 25 indicate 10 mm, 15 mm, 20 mm and 25 mm sample diameter groups.

In conclusion, the purpose of this thesis was the investigation on how the geometry could affect the mechanical properties of cylindrical gels undergoing torsion. This study demonstrates that even with small geometries, such as 10 mm diameter samples, the results are valid. It would be interesting to find out which is the limit for the geometry, that is which is the last sample diameter able to produce significant results. This information might be really useful during brain matter testing because usually the available biological tissue is limited and so more samples could be extracted from the same amount of brain tissue.

Acknowledgements

First of all, I would like to thank my supervisors Luigi Preziosi, professor in Mathematical Engineering in the department of Mathematical Sciences "G. L. Lagrange" at Politecnico di Torino, and, in particular, Valentina Balbi, lecturer in Industrial and Applied Mathematics in the department of Mathematics and Statistics at the University of Limerick, for their fundamental support during the last months.

My deepest gratitude goes to Michel Destrade, Chair of Applied Mathematics in NUI Galway, for welcoming me in Ireland. I would like to thank also James Blackwell and Yangkun Du, PhD students in NUIG, for their help with the testing sessions and numerical simulations.

Bibliography

- [1] M Hrapko et al. “The influence of test conditions on characterization of the mechanical properties of brain tissue”. In: *Journal of Biomechanical Engineering* 130.3 (2008).
- [2] Badar Rashid, Michel Destrade, and Michael D Gilchrist. “Experimental characterisation of neural tissue at collision speeds”. In: *IRCOBI Conference 2012, 12-14 September 2012, Dublin (Ireland)*. International Research Council on the Biomechanics of Injury. 2012.
- [3] S Ganpule et al. “Effect of bulk modulus on deformation of the brain under rotational accelerations”. In: *Shock waves* 28.1 (2018), pp. 127–139.
- [4] Valentina Balbi et al. “Poynting effect of brain matter in torsion”. In: *Soft matter* 15.25 (2019), pp. 5147–5153.
- [5] Badar Rashid, Michel Destrade, and Michael D Gilchrist. “Mechanical characterization of brain tissue in simple shear at dynamic strain rates”. In: *Journal of the mechanical behavior of biomedical materials* 28 (2013), pp. 71–85.
- [6] Svein Kleiven. “Why most traumatic brain injuries are not caused by linear acceleration but skull fractures are”. In: *Frontiers in bioengineering and biotechnology* 1 (2013), p. 15.
- [7] Svein Kleiven. “Evaluation of head injury criteria using a finite element model validated against experiments on localized brain motion, intracerebral acceleration, and intracranial pressure”. In: *International Journal of Crashworthiness* 11.1 (2006), pp. 65–79.
- [8] Cindy L Stanfield et al. *Principles of human physiology*. Benjamin Cummings, 2011.
- [9] *Overview of Cerebral Function*. 2019. URL: <https://www.merckmanuals.com/professional/neurologic-disorders/function-and-dysfunction-of-the-cerebral-lobes/overview-of-cerebral-function>.
- [10] Nadine Abelson-Mitchell. “Epidemiology and prevention of head injuries: literature review”. In: *Journal of clinical nursing* 17.1 (2008), pp. 46–57.

- [11] Tresa Roebuck-Spencer and Alison Cernich. "Epidemiology and societal impact of traumatic brain injury". In: *Handbook on the neuropsychology of traumatic brain injury*. Springer, 2014, pp. 3–23.
- [12] Angela L Marr and Victor G Coronado. "Central nervous system injury surveillance data submission standards—2002". In: *Atlanta, GA: US Department of Health and Human Services, CDC* (2004).
- [13] QUALIFYING STATEMENTS. "VA/DoD clinical practice guideline for management of concussion/mild traumatic brain injury". In: *J Rehabil Res Dev* 46.6 (2009).
- [14] Christopher S Sahler and Brian D Greenwald. "Traumatic brain injury in sports: a review". In: *Rehabilitation research and practice* 2012 (2012).
- [15] Justification Concussion. "Practice Parameter". In: *Neurology* 48 (1997), pp. 581–585.
- [16] W Ritchie Russell and Aaron Smith. "Post-traumatic amnesia in closed head injury". In: *Archives of neurology* 5.1 (1961), pp. 4–17.
- [17] J Head. "Definition of mild traumatic brain injury". In: *J Head Trauma Rehabil* 8.3 (1993), pp. 86–87.
- [18] Christopher C Giza and Jeffrey S Kutcher. "An introduction to sports concussions". In: *CONTINUUM: Lifelong Learning in Neurology* 20.6 Sports Neurology (2014), p. 1545.
- [19] David F Meaney, Barclay Morrison, and Cameron Dale Bass. "The mechanics of traumatic brain injury: a review of what we know and what we need to know for reducing its societal burden". In: *Journal of biomechanical engineering* 136.2 (2014).
- [20] Thomas A Gennarelli. "Head injury in man and experimental animals: clinical aspects". In: *Trauma and regeneration*. Springer, 1983, pp. 1–13.
- [21] Douglas H Smith, David F Meaney, and William H Shull. "Diffuse axonal injury in head trauma". In: *The Journal of head trauma rehabilitation* 18.4 (2003), pp. 307–316.
- [22] Mark Faul et al. "Traumatic brain injury in the United States; emergency department visits, hospitalizations, and deaths, 2002-2006". In: (2010).
- [23] Victor G Coronado et al. "Traumatic brain injury epidemiology and public health issues". In: *Brain injury medicine: Principles and practice* 84 (2012).
- [24] Anbesaw W Selassie et al. "Incidence of long-term disability following traumatic brain injury hospitalization, United States, 2003". In: *The Journal of head trauma rehabilitation* 23.2 (2008), pp. 123–131.

- [25] Eduard Zaloshnja et al. "Prevalence of long-term disability from traumatic brain injury in the civilian population of the United States, 2005". In: *The Journal of head trauma rehabilitation* 23.6 (2008), pp. 394–400.
- [26] Jean A Langlois, Wesley Rutland-Brown, and Marlina M Wald. "The epidemiology and impact of traumatic brain injury: a brief overview". In: *The Journal of head trauma rehabilitation* 21.5 (2006), pp. 375–378.
- [27] Michel Destrade and Ray Ogden. "Nonlinear elasticity". 2010.
- [28] Yuan-cheng Fung. *Biomechanics: mechanical properties of living tissues*. Springer Science & Business Media, 2013.
- [29] Joan O'Connor Blanco et al. "FINITE GROWTH IN TERMOELASTIC MATERIALS". In: (2013).
- [30] Simon Chatelin, André Constantinesco, and Rémy Willinger. "Fifty years of brain tissue mechanical testing: from in vitro to in vivo investigations". In: *Biorheology* 47.5-6 (2010), pp. 255–276.
- [31] *Firmer, Fitter Frame Linked to Firmer, Fitter Brain*. URL: <http://neurosciencenews.com/brain-body-fitness-7311/>.
- [32] Badar Rashid, Michel Destrade, and Michael D Gilchrist. "Inhomogeneous deformation of brain tissue during tension tests". In: *Computational Materials Science* 64 (2012), pp. 295–300.
- [33] Karol Miller and Kiyoyuki Chinzei. "Mechanical properties of brain tissue in tension". In: *Journal of biomechanics* 35.4 (2002), pp. 483–490.
- [34] Michel Destrade et al. "Extreme softness of brain matter in simple shear". In: *International Journal of Non-Linear Mechanics* 75 (2015), pp. 54–58.
- [35] Farhana Pervin and Weinong W Chen. "Mechanically similar gel simulants for brain tissues". In: *Dynamic Behavior of Materials, Volume 1*. Springer, 2011, pp. 9–13.
- [36] URL: <https://www.anton-paar.com/it-it/prodotti/dettagli/reometri-mcr-102-302-502/>.
- [37] Pasquale Ciarletta and Michel Destrade. "Torsion instability of soft solid cylinders". In: *The IMA Journal of Applied Mathematics* 79.5 (2014), pp. 804–819.